

Mechanical Valves for On-Board Flow Control of Inflatable Robots

Lishuai Jin, Antonio Elia Forte, and Katia Bertoldi*

Inflatable robots are becoming increasingly popular, especially in applications where safe interactions are a priority. However, designing multifunctional robots that can operate with a single pressure input is challenging. A potential solution is to couple inflatables with passive valves that can harness the flow characteristics to create functionality. In this study, simple, easy to fabricate, lightweight, and inexpensive mechanical valves are presented that harness viscous flow and snapping arch principles. The mechanical valves can be fully integrated on-board, enabling the control of the incoming airflow to realize multifunctional robots that operate with a single pressure input, with no need for electronic components, cables, or wires. By means of three robotic demos and guided by a numerical model, the capabilities of the valves are demonstrated and optimal input profiles are identified to achieve prescribed functionalities. The study enriches the array of available mechanical valves for inflatable robots and enables new strategies to realize multifunctional robots with on-board flow control.

1. Introduction

From minimally invasive surgical tools^[1–4] and assistive devices,^[5–8] to compliant grippers^[9–12] and video game add-ons,^[13–15] inflatable soft robots have claimed an entire domain of applications for which safe interactions with the surrounding environment is the priority.^[16–19] They are inherently compliant, easy to fabricate, and able to achieve complex motions harnessing the input pressure. However, the control of the fluid flow typically requires complex infrastructures comprising power sources, solenoid valves, electronic circuits, and pumps. As such, the development of strategies for an efficient actuation and

control of inflatable soft robots is essential to the advancement of the field. Toward this end, various principles have been investigated to achieve flow control through pneumatic valves: flapping membranes inside the airways,^[20–22] collapsing soft channels,^[23–27] and kinks in soft tubes.^[28,29] In addition, the snapping of bistable elastomeric membranes has recently been employed to design soft valves that use a second pressure signal to switch between states^[28,30–32]—the first of their kind to be built entirely from soft materials and to operate without the need of electronics. Such valves have demonstrated to provide a platform for the design of logic elements,^[30] ring oscillators that induce periodic motion using constant-pressure,^[31] as well as electronics-free pneumatic circuits for controlling soft-legged robots.^[32]

The design of mechanical valves that can be integrated into soft robots and operated without the needs of additional inputs is, however, still at an early stage. A more extensive library of elements would be ideal in order to expand the capabilities of soft robots that can operate without the need of electronic components.

Inspired by the recent progress in the design of mechanical valves, here we use different strategies to design and realize simple, easy to fabricate, lightweight and inexpensive mechanical valves, that are driven by the same pressure input used for the robot's actuation. Our designs harness both viscous flow and snapping arch principles, can be fully integrated on-board and enable the control of the incoming airflow to realize multifunctional robots that operate with a single pressure input and no need for electronic components. These include a soft robotic arm capable of achieving multiple trajectories, a robot capable of climbing vertically in a tube carrying two times its own weight and even grasping an object and pulling it down, and a rolling robot that can successfully navigate in two directions.

2. Our Mechanical Valves

To simplify the flow control in soft robots, we design, realize, and test four fluidic mechanical valves. The first design, which we refer to as viscous valve, uses a narrow tube with length $l_{tube} = 25$ mm and internal diameter $d_{tube} = 0.21$ mm to provide a transient pressure difference between adjacent actuators (**Figure 1a**) and causes their sequential activation. To demonstrate the capability of this valve we place it between a rigid chamber and

L. Jin, A. E. Forte, K. Bertoldi
John A. Paulson School of Engineering and Applied Sciences
Harvard University
Cambridge, MA 02138, USA
E-mail: bertoldi@seas.harvard.edu

A. E. Forte
Department of Electronics
Information and Bioengineering, Politecnico di Milano
Milan 20133, Italy

 The ORCID identification number(s) for the author(s) of this article can be found under <https://doi.org/10.1002/advs.202101941>

© 2021 The Authors. Advanced Science published by Wiley-VCH GmbH. This is an open access article under the terms of the Creative Commons Attribution License, which permits use, distribution and reproduction in any medium, provided the original work is properly cited.

DOI: 10.1002/advs.202101941

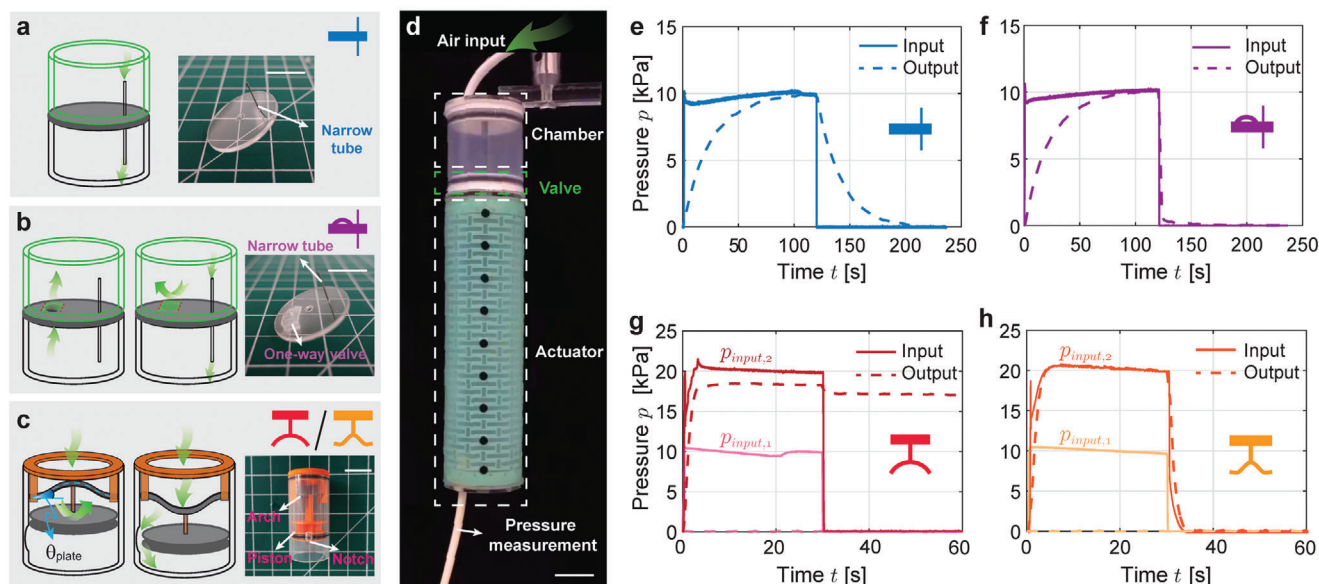


Figure 1. Design and characterization of the mechanical valves. a–c) Schematics and experimental snapshots of the valves. a) The viscous valve (indicated by the blue icon) consists of a acrylic plate and a narrow tube with length $l_{tube} = 25$ mm and inner diameter $d_{tube} = 0.21$ mm. b) The one-way viscous valve (indicated by the purple icon) is a viscous valve with an additional one-way gate which cause a pressure lag only in one direction. c) The hysteretic (indicated by the red icon) and bistable (indicated by the yellow icon) valves exhibit tunable mechanical responses controlled by a snapping arch connected to a movable piston. d) Experimental setup to test the valves. e–h) Pressure evolution at the inlet and outlet of each valve. e) Viscous valve: a delay in the output response in respect to the input is visible in inflation and deflation. f) One-way viscous valve: a delay in the output response in respect to the input is visible only in inflation. g) Hysteretic valve: the on/off thresholds for this valve are ≈ 20 kPa and ≈ 2 kPa, respectively. h) The bistable valve only needs energy to switch its on/off state and would maintain that state once it actuated. Scale bars = 15 mm.

a kirigami-based soft actuator^[33] (Figure 1d). We then supply the chamber with air pressurized at $p_{input} = 10$ kPa for $t_{input} = 120$ s and monitor the pressure evolution inside the soft actuator, p_{output} . As shown in Figure 1e, the valve introduces a transient pressure difference between the chamber and the actuator and that it takes ≈ 100 s for p_{output} to stabilize to p_{input} during both inflation and deflation (see Sections S1.1, S1.2, and S2.1, Supporting Information for additional details about design/fabrication of all our mechanical valves, fabrication of the kirigami actuator and testing, respectively).

The second design is similar to the first one, with the exception of an additional, larger hole ($d_{hole} = 3$ mm) placed next to the narrow tube. This aperture is covered on the top by a soft elastomeric membrane (10 mm long and 6 mm wide) fixed at the two opposite edges (Figure 1b). Such membrane acts like a gate: it can be bent out of plane by an upward airflow but it stays shut against a downward flow. Hence, as shown in Figure 1f, this design functions as a one-way viscous valve and introduces a transient pressure difference only during inflation.

While our first two valves harness viscous flow, we also exploit the snapping and bistability of elastic arches to realize on/off valves. We first form an arch by buckling a metallic plate of length $l_{plate} = 17.5$ mm, width $w_{plate} = 5$ mm and thickness $t_{plate} = 0.075$ mm while constraining the rotation at its two ends. We then slide the ends of the buckled plate into two slits oriented at an angle $\theta_{plate} = 45^\circ$ with respect to the horizontal direction situated at the opposite sides of a 3D-printed plastic holder (Figure S1c, Supporting Information). Next, we connect the center of the buckled plate to a 3D-printed piston, with head diameter of $d_{disk} = 22$ mm. Finally, we insert the system into a cylindri-

cal plastic chamber with inner diameter equal to that of the piston head (i.e., $d_{chamber} = d_{disk}$) to separate it into two volumes and place two O-rings at the top of the holder and around the piston (Figure 1c), to ensure sealing during operation. Importantly, the chamber presents a small, dome-shaped notch on its internal surface (with depth around 1 mm and diameter around 5 mm). Initially, when the arch is curved upward, the head of the piston is located above the notch. In this configuration the airflow is obstructed and p_{output} remains zero. As an example, if the input is a rectangular pulse with magnitude $p_{input,1} = 10$ kPa, the valve remains closed and $p_{output} = 0$ (see light red line in Figure 1g). Differently, if $p_{input,2} \approx 20$ kPa the arch snaps and inverts its curvature, carrying the piston's head across the notch. In this second configuration the fluid in the two separate volumes of the chamber can exchange through the notch. However, the arch behaves hysteretically and snaps back when the pressure difference between the two sides of the piston is smaller than ≈ 2 kPa. As a consequence, the piston travels back across the notch, turning the valve off. This results in a steady pressure offset between the inlet and outlet. Even after the input pressure is removed, the pressure inside the kirigami actuator is kept at such steady level by the valve, so that the actuator remains inflated.

Further, by simply varying the mounting angle θ_{plate} to 0° one can transform the hysteretic valve into a bistable one, which switches state and remains open even when the input pressure is removed. To realize such bistable valve and have it operating at around 20 kPa, we reduce the thickness of the metallic plate to $t_{plate} = 0.05$ mm (while keeping $l_{plate} = 17.5$ mm and $w_{plate} = 5$ mm). This arch remains curved upwards for $p_{input} < 20$ kPa. Therefore, for low pressure inputs the measured outlet pressure

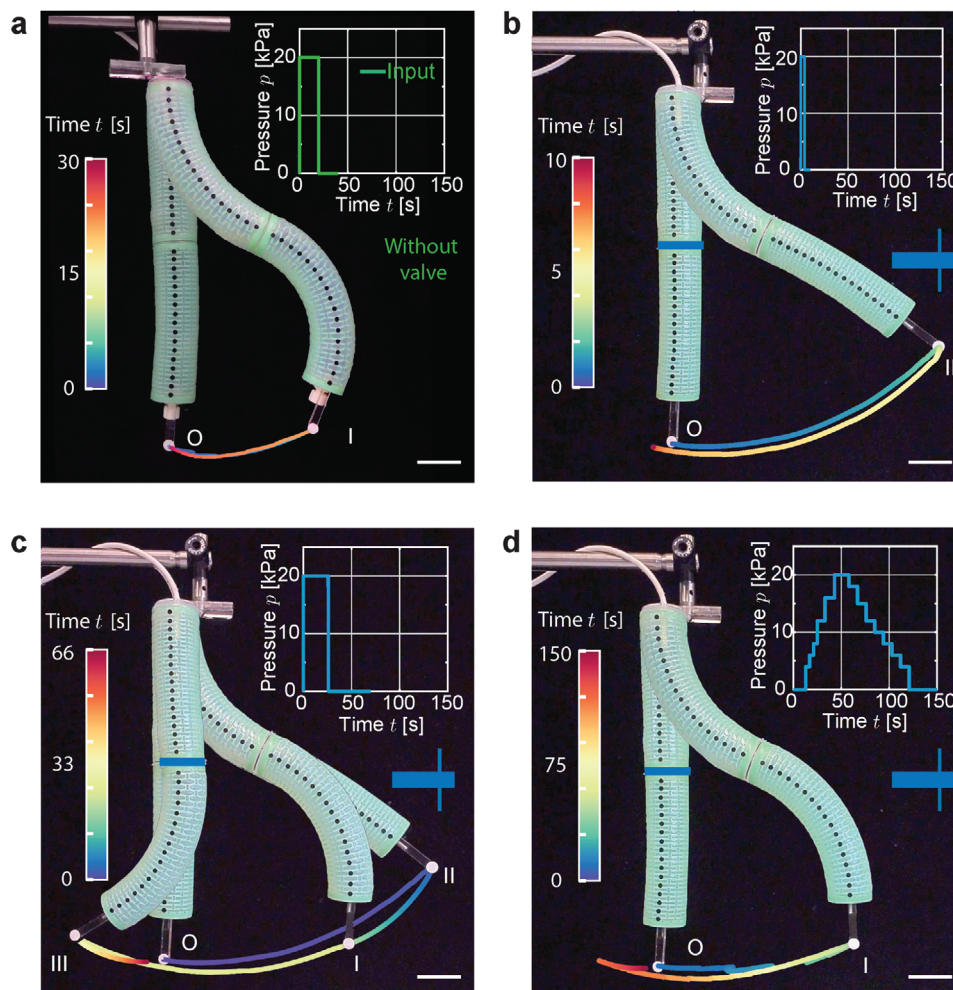


Figure 2. Robotic arm achieving different trajectories. a) A robotic arm comprising two bending actuators with no valve in between them bends to a S-shape when a rectangular pressure pulse is applied ($p_{input} = 20$ kPa for $t_{input} = 20$ s). b–d) By introducing a viscous valve between the two actuators, the trajectory of the arm's tip can be regulated by varying the pressure-time profile in input. b) The endpoint of this robotic arm moves further away compared to the previous version when pressurized ($p_{input} = 20$ kPa for $t_{input} = 4$ s), reaching position II (196 mm away from the initial position), and immediately back to the initial position when the pressure is removed. c) When a longer rectangular pressure pulse is fed to the robot ($p_{input} = 20$ kPa for $t_{input} = 26$ s) the end point of the robotic arm is able to reach three different positions. d) When undergoing to a gradually changed pressure, the robotic arm deforms to an S-shape, resembling the same deformation of the arm without valve. Scale bars = 30 mm.

is equal to zero (see results in Figure 1h for $p_{input,1} = 10$ kPa). However, if the input pressure goes over $p_{input,2} = 20$ kPa, the arch snaps to its inverted stable state and the valve opens (see dark orange line in Figure 1h). Importantly, our bistable valve remains in the opened state even after the input pressure is removed, resulting in a synchronous pressure variation between the input and output (i.e., once the input is removed, the output drops to zero at the same time). A large negative pressure impulse is needed to close this valve (see Figure S14, Supporting Information for additional details about the effect of geometric parameters on the snapping response of our hysteretic and bistable valves).

3. Robotic Arm with Different Trajectories

After introducing our four mechanical designs, we now show how to integrate them with several actuators and realize multi-functional robotic systems powered by a single pressure input.

As a first example, we combine two bending kirigami actuators and a viscous valve to realize a robotic arm that can assume different trajectories by varying a single pressure input. As a reference, in the case of the two actuators simply connected without a valve in between, the robotic arm starts straight and morphs into an S-shape upon application of a rectangular pressure pulse ($p_{input} = 20$ kPa for $t_{input} = 20$ s, see inset in Figure 2a). The actuator's tip reaches a point 102 mm away from the initial position when fully pressurized (I in Figure 2a) and goes back to its initial configuration when the pressure returns to 1 atm (Figure 2a). Clearly, for such robotic arm the deformation is only affected by the magnitude of p_{input} . However, by introducing a viscous valve between the two actuators we can control the trajectory of the tip by modulating the pressure-time profile in input (see Figure 2b–d). To demonstrate the concept, we power the new version of the robotic arm with a short rectangular pressure pulse ($p_{input} = 20$ kPa for

$t_{input} = 4$ s, see the inset of Figure 2b). This results in the top actuator deforming instantaneously upon pressurization, whereas the presence of the viscous valve delays the activation of the bottom one. Therefore, the endpoint of this robotic arm moves further away compared to the previous version when pressurized (reaching position II, 196 mm away from the initial position) and immediately back to the initial position when the pressure is removed. If a longer rectangular pressure pulse is fed to the robot ($p_{input} = 20$ kPa for $t_{input} = 26$ s, see the inset of Figure 2c), the end point of the robotic arm is still able to reach position II during the first few seconds of the cycle. However, as time increases, the bottom actuator also bends, so that the robotic arm gradually mutates into the S-shape configuration, and the endpoint moves to position I. Further, when the input pressure is removed (i.e., for $t_{input} > 26$ s), the top and bottom actuators cannot deflate simultaneously due to the presence of the valve. Consequently, when the top actuator goes back into the initial, straight position, the bottom one is still bent: the endpoint reaches a new position III (65 mm apart from position O) on the left side of the initial configuration before returning to the rest position. Finally, a similar trajectory to that obtained in the absence of the viscous valve can be achieved, by gradually varying the pressure (p_{input} increases from 0 to 20 kPa in 50 s and then decreases to 0 kPa in 100 s—Figure 2d). Note that in this case a left swing is observed at the end of the cycle. This is due to the step-like nature of the pressure input, and can be eliminated by using a smoother pressure input (see Sections S1.3 and S2.3, Supporting Information for additional details about fabrication and testing of the robotic arm).

Whereas in Figure 2 we consider a robotic arm with a viscous valve, the range of achievable trajectories can be further enlarged by incorporating a one-way viscous valve (Figure S17, Supporting Information) and connecting more than two actuators (Figures S18 and S19, Supporting Information). Finally, the behavior of the robotic arm under different pressure inputs can be nicely captured by a simple numerical model based on the Navier–Stokes equations,^[34] expanded to take into account air compressibility (see Section S3.1, Supporting Information for additional details about the model).

4. Tube Climbing Robot

Thus far, we have demonstrated the capabilities of individual valves (viscous and one-way viscous valve) for the realization of a robotic arm with tip trajectories that can be prescribed by modulating the input pressure. As second demonstration we combine different valves together and realize a robot capable of climbing vertically in a pipe. Moreover, the robot can carry twice its own weight and even grasp an object. Differently from previous tube-climbing robots,^[35–38] our system operates with a single pressure input.

To realize such robot we connect two expanding kirigami actuators to an extending one via a one-way viscous valve and a viscous valve (Figure 3a). Upon pressurization, the bottom actuator expands instantaneously and grips onto the pipe (Figure 3b). At the same time the top and middle actuators deform gradually due to the presence of the viscous valves. This results in the head of the robot moving upwards before the top actuator is able to grip onto the pipe. As the pressure input is removed, the top actuator

remains fully inflated, due to the lag introduced by the viscous valve, and acts as anchoring point. Differently, due to the presence of the one-way viscous valve which offers negligible resistance for the air to instantaneously escape, the middle and bottom actuators deflate synchronously. With the top actuator still anchored, the deflation translates in an upward movement for the lower part of the robot, which closes the loop.

Note that such deformation sequence is promising toward enabling a climbing motion, since it is asymmetric and makes the robot extend upwards. However, it only translates into vertical climbing if the frictional force between the inflated top actuator and the tube is i) larger than the weight of the robot (or it will fall) and ii) smaller than the axial extension force generated by the middle actuator (or it will not extend upwards). Since the friction and extension force are dependent on the pressure in each actuator, a tailored input pressure signal is crucial for the ability of the robot to climb. In order to identify input signals that enable climbing, we first measure i) the evolution of the friction between the pipe and the expanding actuator and ii) the extension force generated by the middle actuator as a function of the internal pressure. As shown in Figure 3c, we find that the minimum pressure inside the expanding top actuator should be larger than $p_{low} = 2.5$ kPa to prevent slipping and smaller than $p_{high} = 4.2$ kPa to enable axial extension toward the top.

To identify a suitable input signal that satisfy these requirements, we run 77 numerical analysis where we systematically vary p_{input} and t_{input} (with $p_{input} \in [7, 19]$ kPa and $t_{input} \in [38, 58]$ s) while keeping the actuation period equal to $T = 60$ s. In Figure 3d, we report the minimum pressure recorded for the top actuator after the first cycle, p_{min} , as a function of p_{input} and t_{input} . Within the explored design space we find a “climbing” region (bounded by the two dashed lines) for which p_{min} is greater than p_{low} and smaller than p_{high} . To validate these numerical predictions, we conduct experiments in which we provide an input pressure of $p_{input} = 13$ kPa and select t_{input} guided by the results of Figure 3d. Note that in order to maximize the extension toward the top of the middle actuator and, in turn, increase the efficiency of the robot, for a given value of p_{input} , t_{input} should be selected to be as close as possible to the lower boundary of the “climbing” region. In fact, the closer we operate to the lower boundary, the greater is the difference between the vertical extension force exerted by the middle actuator and the friction between top actuator and the tube (Figure 3c, red segment). As such, we first choose $t_{input} = 45$ s (Figure S20a, Supporting Information). However, because of small discrepancies between our experiments and model (which slightly over predicts the minimum pressure in the top actuator—Figure 3e), we find that the frictional force is not enough to prevent falling. Therefore, we increase t_{input} to 48 s to move slightly away from the lower boundary of the domain and find that for this input the robot climbs upwards and moves of 13 cm in 25 cycles (Figure 3f). In Figure 3e, we report the resultant input pressure profile fed into the bottom actuator of the robot (green curve), along with the pressure profiles measured in all the chambers (continuous lines) and those predicted by the model (dashed lines) and find very good agreement between the two sets of data. Further, these results are in agreement with the predicted climbing sequence shown in Figure 3b. In fact, when p_{input} is removed, the pressure decreases in all three actuators. However, while this drop is almost instantaneous in the

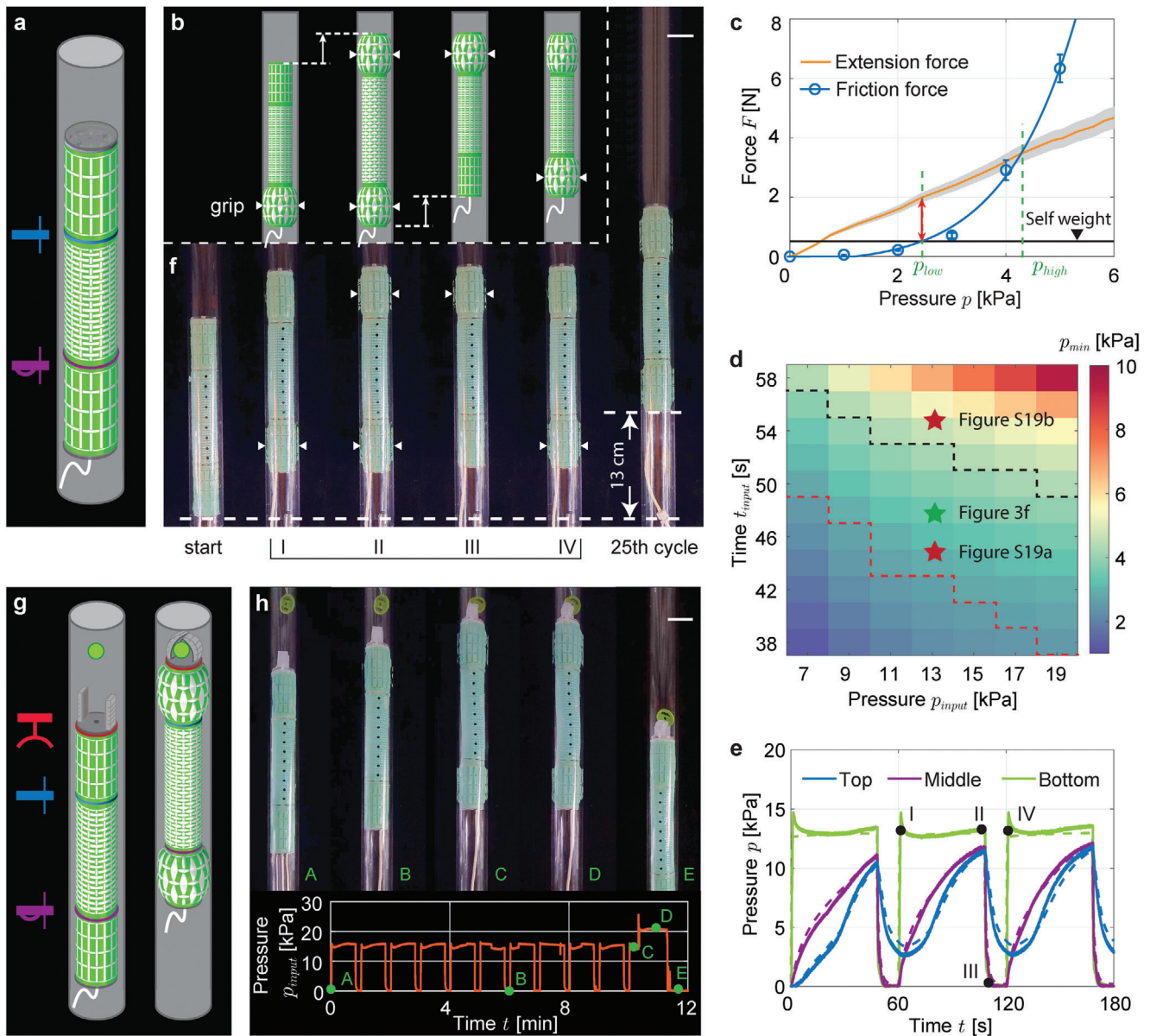


Figure 3. Multifunctional climbing robot. a) Schematic of the climbing robot comprising three kirigami actuators (two expanding and one extending actuator), a one-way viscous valve and a viscous valve. b) Climbing of the robot is enabled by the sequential inflation and deflation of the actuators, which can be modulated by varying the pressure-time profile of a single pressure input. c) The evolution of the friction between the pipe and the expanding actuator as well as the extension force generated by the middle actuator, as a function of the internal pressure. According to the plots, the minimum pressure inside the expanding top actuator should be larger than $p_{low} = 2.5$ kPa to prevent slipping and smaller than $p_{high} = 4.2$ kPa to enable axial extension toward the top. Error bars indicate the standard deviation for the measurements. d) Phase diagram of the minimum pressure inside the top actuator (after the first cycle). The area of the diagram that is bounded by the two dashed lines identifies the input parameters for which the robot will achieve climbing. e) Comparison between the experimental and numerical results of the pressure evolution inside the actuators. The good agreement between them enables one to predict the behavior of the robot using the numerical model. f) Experimental demonstration of the climbing robot which climbs 13 cm in 25 cycles with $p_{input} = 13$ kPa, $t_{input} = 48$ s and $T = 60$ s. g) Schematic of the climbing robot capable of grasping an object and pulling it down, which is realized by adding an additional hysteretic valve and gripper to the top actuator. h) Experimental snapshots of the climbing robot with the gripper. Scale bars = 30 mm.

bottom and middle actuator, it is less sharp in the top one due to the delay introduced by the viscous valve. Importantly, this results in a non-zero minimum pressure for the top actuator, which enables upward retraction of the other two chambers while assuring anchoring. Additionally, it is worth noticing that if t_{input}

is further increased to 55 s, the robot does not move upwards as the frictional force between the top actuator and the pipe becomes too large (Figure S20b, Supporting Information). Further, we note that, using the same approach, the input signal can be also optimized to make the robot carrying two time its weight

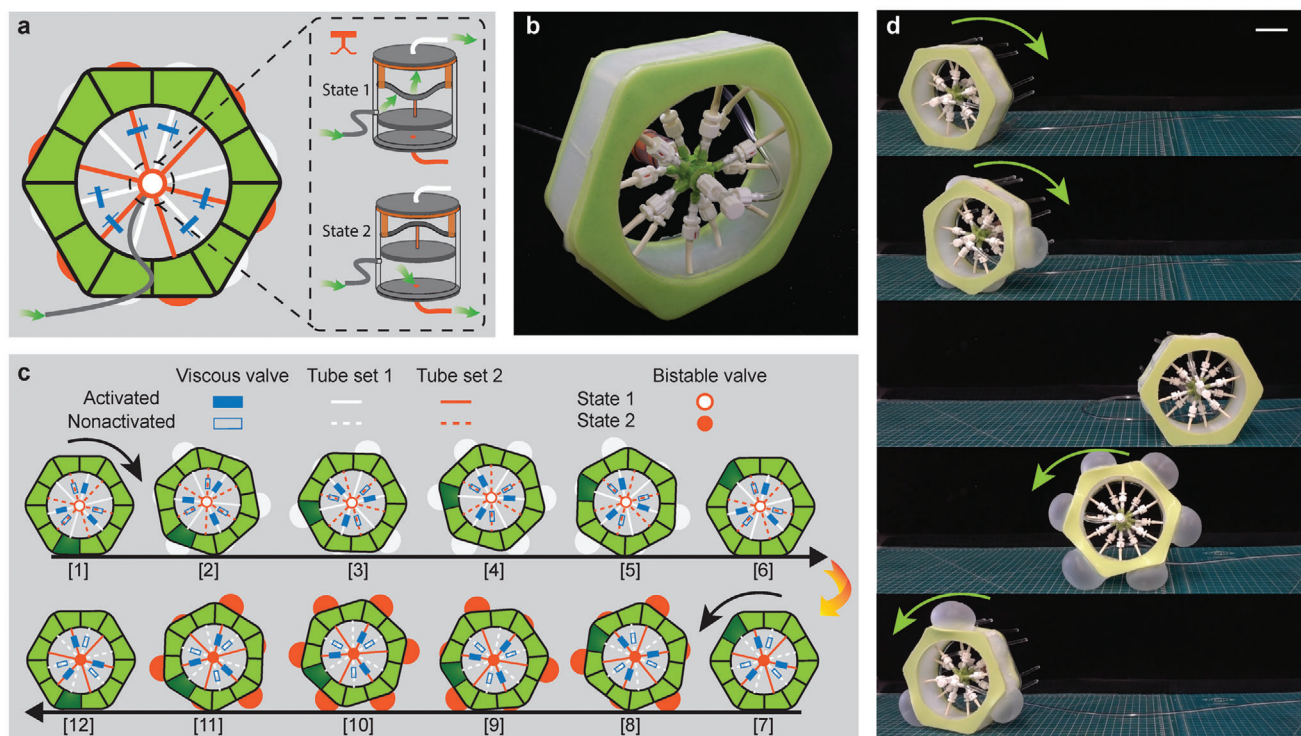


Figure 4. Rolling robot. a) A hexagonal rolling robot integrated with a modified version of the bistable valve and six viscous valves is able to roll bi-directionally with a single pressure input. The bistable valve has two states, which allow it to dispense the input flow into two separate circuits, each connecting six chambers (highlighted in white and orange). Each circuit has three chambers connected directly to the bistable valve, while other three chambers are connected to the bistable valve through viscous valves. b) Experimental snapshots of the rolling robot. c) Operating principle of the rolling robot. The chambers on the rolling robot inflate/deflate sequentially due to the presence of viscous valves pushing the robot away from one face to another. The bistable valve, which can be switched by applying a pressure burst, dispenses the input flow into different circuits enabling the bi-directional rolling. d) Experimental snapshots of the robot rolling in both directions. Scale bars = 50 mm.

(Figure S20d and Movie S3, Supporting Information). Finally, we want to emphasize that the slow speed of the robot is due to the low flow rate of our input pump (ITV1030 by SMC Cooperation, with flow rate around 7.5 mL s^{-1} at pressure of 20 kPa) rather than our mechanical valves and that the speed could be largely increased by using a better input pump to increase the flow rate (Figure S22, Supporting Information).

Next, to enhance the functionality of the robot and making it capable of grasping an object and pulling it down, we add a gripper to its head (comprising two PneuNets^[9]) and connect it to the top actuator via an hysteretic valve (Figure 3g). Since the valve is embedded into the top actuator, it affects the actuator's pressure-volume relationship and, in turn, alters the input parameters required for climbing. Therefore we rerun the numerical analysis accounting for the internal volume reduction of the top actuator and find that larger values of p_{input} are required to achieve locomotion (Figure S21, Supporting Information). Guided by the numerical analyses we then choose $p_{input} = 15 \text{ kPa}$ and $t_{input} = 48 \text{ s}$. As shown in Figure 3h, we find that, when $p_{input} = 15 \text{ kPa}$ is cyclically applied, the robot navigates upwards toward the object. Then, as the robot approaches the object, a pressure higher than the threshold pressure of the hysteretic valve ($p_{input} = 22 \text{ kPa}$) is supplied (the input pressure profile for the experiments is reported in the bottom panel of Figure 3h). The valve opens and actuate the gripper, which grasps the object in the pipe. After-

wards, when the pressure in the gripper approaches the pressure inside the top actuator, the hysteretic valve snap back, switching off. At this point, the gripper remains inflated, keeping hold of the object. Finally, the three kirigami actuators can be deflated to remove the anchoring points and let the robot slide down with the captured object.

5. Rolling Robot

To further illustrate the capability of our valves, we design and test a hexagonal rolling robot integrated with one bistable valve and six viscous valves. This robot is different from other rolling robots^[31,39–42] due to its ability to roll bi-directionally with a single pressure input. The robot comprises twelve inflatable chambers evenly distributed along the perimeter of an hexagon (two on each side, see Figure 4a,b). Such chambers act as legs and by selectively inflating and deflating them we can push the robot away from a stable equilibrium and make it roll forward or backward.

Such rolling motion can be realized with a single input pressure by introducing viscous valves. More specifically, we form a circuit connecting six inflatable chambers and the input source (white connections in Figure 4a). Three of these chambers are connected directly to the pressure supplier. Alternating these, there are three additional chambers, each of which is connected to a viscous valves before being connected to input

(see schematics in Figure 4a). When a pressure input is supplied, the chambers directly attached to the input valve inflate first (snapshot 2 in Figure 4c). This unbalances the robot to the point that it rolls over the hexagon's corner and lay flat on an edge where the chamber is still deflated (snapshot 3 in Figure 4c). At this point the chambers attached to the viscous valves, which suffer an inflation delay, start to inflate too (snapshot 4 in Figure 4c). When the input pressure is removed, the chambers with no viscous valve deflate instantaneously, while the ones with viscous valves keep the inflated state temporarily and push the robot to rotate further (snapshot 5 in Figure 4c) until all the chamber deflate to the initial state (snapshot 6 in Figure 4c). The robot can keep rotating forward by repeating the aforementioned procedure. Note that, in an effort to speed up the locomotion, in this demonstration the diameter of the viscous valves's narrow tube was increased to $d_{tube}=0.26$ mm.

Further, the direction of rolling can be changed by introducing an identical circuit that connects the remaining six chambers and a slightly modified design of the bistable valve in which the notch is replaced with a hole with diameter of 1.6 mm. When the input source is connected to this hole (see schematics in Figure 4a), the new version of the bistable valve is able to switch the flow from one circuit to the other (highlighted in white and orange in Figure 4a). This is possible by applying a negative pressure burst to the input to snap the arch and, in turn, change the position of the piston. The piston travels over the hole and switches the valve's output to the second circuit (orange tubes), where the inflatable chambers are positioned in the opposite order. The robot can then start rotating in the opposite direction by repeating the same inflation cycle (snapshots 7–12 in Figure 4c).

To demonstrate the concept experimentally we fabricate a prototype out of elastomeric materials by means of a molding approach. From the experimental snapshots in Figure 4d, we can see that the robot rolls from one face of the hexagonal frame to the next as the chamber on each face sequentially inflate and deflate. Further, by applying a negative pressure pulse ($p_{input} = -25$ kPa, see Figure S11 and Movie S4, Supporting Information) we can switch the state of the bistable valve and change the direction of rolling.

6. Conclusion

In summary, we have designed and built simple, easy to fabricate, lightweight, and inexpensive mechanical valves that can be easily integrated with soft actuators to control the airflow and realize robotic systems that operate with a single pressure input. Our mechanical valves provide new opportunities to realize sequential operation robots, and enrich the array of existing valves. Specifically, while the large majority of the existing designs require an external input to operate—including soft bistable valves,^[28] thermal responsive microvalves,^[20] and microfluidic devices^[23,24]—our valves are fully passive and easy to integrated on-board, facilitating the design of robots that can selectively activate different parts, depending on the application. Further, while most previously proposed designed are on/off valves,^[25,28,29] our viscous valves can generate flow resistance in symmetric or asymmetric ways, enabling the design of robots with sequential operation. While in this study we have demonstrated the potential of our valves by using kirigami fluidic actu-

ators, our devices can interface with any type of pneumatic soft actuator to control the incoming airflow and realize robots that operate with a single pressure input. Further, besides the three robotic demos presented here, our devices hold potential to be employed in various robotic systems in the future. For example, by integrating a viscous and hysteretic valve together, we could design a new valve that offers a pressure lag when supplying low pressure (lower than the threshold of the arch snapping), while exhibits instant on/off switch when supplying higher pressure. This might enable the design of biomimicking robots capable of switching between different motion modes (e.g., walking and jumping), despite a single input pressure. Finally, one could expand the current study by investigating the behavior of complex systems comprising valves in series and parallel configurations and enrich the array of available valves with new designs harnessing instabilities in compliant shell elements.

Supporting Information

Supporting Information is available from the Wiley Online Library or from the author.

Acknowledgements

K.B. acknowledges support from the National Science Foundation under Grant No. DMR-2011754. A.E.F. acknowledges that this project has received funding from the European Union's Horizon 2020 research and innovation programme under the Marie Skłodowska-Curie Grant Agreement No. 798244.

Conflict of Interest

The authors declare no conflict of interest.

Data Availability Statement

The data that support the findings of this study are available from the corresponding author upon reasonable request.

Keywords

climbing, mechanical valves, robotic arm, rolling, soft robots

Received: May 9, 2021

Revised: July 3, 2021

Published online:

- [1] M. Cianchetti, T. Ranzani, G. Gerboni, T. Nanayakkara, K. Althofer, P. Dasgupta, A. Menciassi, *Soft Robot.* **2014**, *1*, 122.
- [2] M. A. Horvath, I. Wamala, E. Rytkin, E. Doyle, C. J. Payne, T. Thalhofer, I. Berra, A. Solovyeva, M. Saeed, S. Hendren, E. T. Roche, P. J. D. Nido, C. J. Walsh, N. V. Vasilyev, *Ann. Biomed. Eng.* **2017**, *45*, 2222.
- [3] A. Diodato, M. Brancadoro, G. De Rossi, H. Abidi, D. Dall'Alba, R. Muradore, G. Ciuti, P. Fiorini, A. Menciassi, M. Cianchetti, *Surg. Innov.* **2018**, *25*, 69.
- [4] M. Runciman, A. Darzi, G. P. Mylonas, *Soft Robot.* **2019**, *6*, 423.

- [5] M. Cianchetti, C. Laschi, A. Menciassi, P. Dario, *Nat. Rev. Mater.* **2018**, 3, 143.
- [6] J. W. Booth, D. Shah, J. C. Case, E. L. White, M. C. Yuen, O. Cyr-Choiniere, R. Kramer-Bottiglio, *Sci. Robot.* **2018**, 3, 22.
- [7] L. Cappello, J. T. Meyer, K. C. Galloway, J. D. Peisner, R. Granberry, D. A. Wagner, S. Engelhardt, S. Paganoni, C. J. Walsh, *J. Neuroeng. Rehabilitation* **2018**, 15, 1.
- [8] L. Ge, F. Chen, D. Wang, Y. Zhang, D. Han, T. Wang, G. Gu, *Soft Robot.* **2020**, 7, 583.
- [9] F. Ilievski, A. D. Mazzeo, R. F. Shepherd, X. Chen, G. M. Whitesides, *Angew. Chem.* **2011**, 123, 1930.
- [10] K. C. Galloway, K. P. Becker, B. Phillips, J. Kirby, S. Licht, D. Tchernov, R. J. Wood, D. F. Gruber, *Soft Robot.* **2016**, 3, 23.
- [11] N. R. Sinatra, C. B. Teeple, D. M. Vogt, K. K. Parker, D. F. Gruber, R. J. Wood, *Sci. Robot.* **2019**, 4, eaax5425.
- [12] Z. Xie, A. G. Domel, N. An, C. Green, Z. Gong, T. Wang, E. M. Knubben, J. C. Weaver, K. Bertoldi, L. Wen, *Soft Robot.* **2020**, 7, 639.
- [13] S. Kim, H. Kim, B. Lee, T.-J. Nam, W. Lee, in *Proceedings of the SIGCHI Conference on Human Factors in Computing Systems*, ACM, New York **2008**, p. 211.
- [14] S.-Y. Teng, T.-S. Kuo, C. Wang, C.-h. Chiang, D.-Y. Huang, L. Chan, B.-Y. Chen, in *Proceedings of the 31st Annual ACM Symposium on User Interface Software and Technology*, ACM, New York **2018**, p. 5.
- [15] S.-Y. Teng, C.-L. Lin, C.-H. Chiang, T.-S. Kuo, L. Chan, D.-Y. Huang, B.-Y. Chen, in *Proceedings of UIST*, ACM, New York **2019**, p. 639.
- [16] D. Trivedi, C. D. Rahn, W. M. Kier, I. D. Walker, *Appl. Bion. Biomech.* **2008**, 5, 99.
- [17] D. Rus, M. T. Tolley, *Nature* **2015**, 521, 467.
- [18] P. Polygerinos, N. Correll, S. A. Morin, B. Mosadegh, C. D. Onal, K. Petersen, M. Cianchetti, M. T. Tolley, R. F. Shepherd, *Adv. Eng. Mater.* **2017**, 19, 1700016.
- [19] B. Shih, D. Shah, J. Li, T. G. Thuruthel, Y.-L. Park, F. Iida, Z. Bao, R. Kramer-Bottiglio, M. T. Tolley, *Sci. Robot.* **2020**, 5, eaaz9239.
- [20] C. Goll, W. Bacher, B. Büstgens, D. Maas, W. Menz, W. Schomburg, *J. Micromech. Microeng.* **1996**, 6, 77.
- [21] N. Napp, B. Araki, M. T. Tolley, R. Nagpal, R. J. Wood, in *IEEE ICRA*, IEEE, Piscataway, NJ **2014**, p. 1440.
- [22] F. B. Coulter, M. Schaffner, J. A. Faber, A. Rafsanjani, R. Smith, H. Appa, P. Zilla, D. Bezuidenhout, A. R. Studart, *Matter* **2019**, 1, 266.
- [23] M. A. Unger, H.-P. Chou, T. Thorsen, A. Scherer, S. R. Quake, *Science* **2000**, 288, 113.
- [24] B. Mosadegh, C.-H. Kuo, Y.-C. Tung, Y.-s. Torisawa, T. Bersano-Begey, H. Tavana, S. Takayama, *Nat. Phys.* **2010**, 6, 433.
- [25] B. Mosadegh, A. D. Mazzeo, R. F. Shepherd, S. A. Morin, U. Gupta, I. Z. Sani, D. Lai, S. Takayama, G. M. Whitesides, *Lab Chip* **2014**, 14, 189.
- [26] P. N. Duncan, S. Ahrar, E. E. Hui, *Lab Chip* **2015**, 15, 1360.
- [27] M. Wehner, R. L. Truby, D. J. Fitzgerald, B. Mosadegh, G. M. Whitesides, J. A. Lewis, R. J. Wood, *Nature* **2016**, 536, 451.
- [28] P. Rothmund, A. Ainla, L. Belding, D. J. Preston, S. Kurihara, Z. Suo, G. M. Whitesides, *Sci. Robot.* **2018**, 3, 16.
- [29] K. Luo, P. Rothmund, G. M. Whitesides, Z. Suo, *J. Mech. Phys. Solids* **2019**, 131, 230.
- [30] D. J. Preston, P. Rothmund, H. J. Jiang, M. P. Nemitz, J. Rawson, Z. Suo, G. M. Whitesides, *Proc. Natl. Acad. Sci. U.S.A.* **2019**, 116, 7750.
- [31] D. J. Preston, H. J. Jiang, V. Sanchez, P. Rothmund, J. Rawson, M. P. Nemitz, W.-K. Lee, Z. Suo, C. J. Walsh, G. M. Whitesides, *Sci. Robot.* **2019**, 4, eaaw5496.
- [32] D. Drotman, S. Jadhav, D. Sharp, C. Chan, M. T. Tolley, *Sci. Robot.* **2021**, 6, eaay2627.
- [33] L. Jin, A. E. Forte, B. Deng, A. Rafsanjani, K. Bertoldi, *Adv. Mater.* **2020**, 32, 2001863.
- [34] N. Vasios, A. J. Gross, S. Soifer, J. T. Overvelde, K. Bertoldi, *Soft Robot.* **2020**, 7, 1.
- [35] J. O. Alcaide, L. Pearson, M. E. Rentschler, in *IEEE ICRA*, IEEE, Piscataway, NJ **2017**, p. 4338.
- [36] M. S. Verma, A. Ainla, D. Yang, D. Harburg, G. M. Whitesides, *Soft Robot.* **2018**, 5, 133.
- [37] W. Adams, S. Sridar, C. M. Thalman, B. Copenhaver, H. Elsaad, P. Polygerinos, in *IEEE RoboSoft*, IEEE, Piscataway, NJ **2018**, p. 321.
- [38] B. Zhang, Y. Fan, P. Yang, T. Cao, H. Liao, *Soft Robot.* **2019**, 6, 399.
- [39] E. Steltz, A. Mozeika, J. Rembisz, N. Corson, H. Jaeger, *Proc. SPIE* **2010**, 7642, 764225.
- [40] A. D. Marchese, C. D. Onal, D. Rus, *International Conference on Intelligent Robots and Systems*, IEEE, Piscataway, NJ **2011**, p. 756.
- [41] S. A. Morin, Y. Shevchenko, J. Lessing, S. W. Kwok, R. F. Shepherd, A. A. Stokes, G. M. Whitesides, *Adv. Mater.* **2014**, 26, 5991.
- [42] H.-Y. Chen, R. S. Diteesawat, A. Haynes, A. J. Partridge, M. F. Simons, E. Werner, M. Garrad, J. Rossiter, A. T. Conn, *Front. Robot. AI* **2019**, 6, 52.



Supporting Information

for *Adv. Sci.*, DOI: 10.1002/adv.202101941

Mechanical Valves for On-Board Flow Control of Inflatable Robots

*Lishuai Jin, Antonio Elia Forte, and Katia Bertoldi**

1 **Supporting Information for**
2 **Mechanical valves for on-board flow control of**
3 **inflatable robots**

4 **Lishuai Jin, Antonio Elia Forte, and Katia Bertoldi**

5 **E-mail: bertoldi@seas.harvard.edu**

6 **This PDF file includes:**

- 7 Figs. S1 to S22
- 8 Tables S1 to S2
- 9 Captions for Movies S1 to S4
- 10 References for SI reference citations

11 **Other supplementary materials for this manuscript include the following:**

- 12 Movies S1 to S4

13 1. Fabrication

14 In this Section we provide details on the fabrication of our mechanical valves as well as the three
15 robotic systems (i.e. the robotic arm, the climbing robot and the rolling robot)

16 **1.1. Mechanical valves.** To simplify the flow control in soft robots, we introduce four fluidic
17 mechanical valves: (i) viscous valve, (ii) one-way viscous valve, (iii) hysteretic valve and (iv)
18 bistable valve.

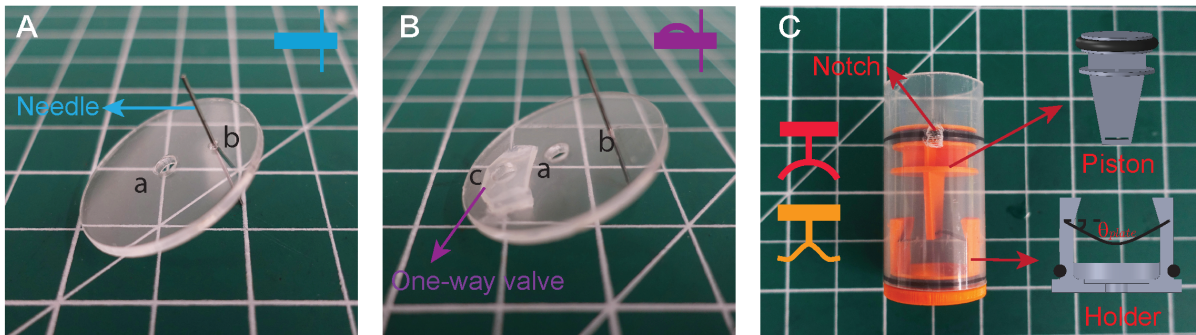


Fig. S1. Design of the mechanical valves. Experimental snapshots of (A) viscous valve, (B) one-way viscous valve and (C) hysteretic or bistable valve.

- 19 • *Viscous valve:* The viscous valve tested in this study comprises a circular acrylic plate with
20 embedded a hollow tube with small diameter (Fig. S1A). Specifically, our viscous valves are
21 fabricated using the following steps
 - 22 – Laser cut a circular acrylic plate with diameter of 30 mm and thickness of 1/16 inch.
 - 23 – Cut two holes in the acrylic plate: (a) one at the center with diameter of 3 mm that is
24 used to connect adjacent actuators via a bolt; and (b) one with smaller diameter of ~ 0.8
25 mm that is used to embed the narrow tube.
 - 26 – Insert a narrow tube through the hole **b** of the acrylic plate and seal the gap between
27 the tube and the hole using glue (Sil-Poxy Silicone Adhesive, Smooth-On). The narrow
28 tubes used in this study are cut from glue needles (FEITA) and have length of 25 mm
29 and inner diameter varying from 0.16 mm to 0.51 mm.
- 30 • *One-way viscous valve:* To obtain a valve with unidirectional pressure drop, we add a one-way
31 valve to the viscous valve described above. Our one-way valves are fabricated using the
32 following steps (Fig. S1B):
 - 33 – Cut another hole (with diameter of 3 mm) on the acrylic plate of the viscous valve
34 (denoted with **c** in Fig. S1B). To avoid conflict when assembling the valve with actuators,
35 this hole is in a diametrically opposite position to the one used for the needle.
 - 36 – Cast a rectangular shape membrane using Ecoflex 00-50 with length of ~ 10 mm, width
37 of ~ 6 mm and thickness of ~ 1 mm.
 - 38 – Glue the two short edges of the membrane on the acrylic plate to cover hole **c**. If the
39 membrane is attached to the top of the plate, it allows only flow from the bottom to the
40 top. In fact the flow bends the membrane and allows the air through hole **c**.

41 Please note that when the valves are integrated with the actuators, the hole in the center of
42 the acrylic plate should be sealed by an appropriate sealing ring to avoid air leaking (see Fig.
43 S3 and S4).

- 44 • *Hysteretic valve*: Our hysteretic valve exploits the snapping of elastic arches (Fig.S1 C). To
45 fabricate the valve, we follow the steps below:
 - 46 – Laser cut rectangular plates with width $w_{plate} = 5$ mm and length $l_{plate} = 17.5$ mm
47 out of 1095 spring steel shims (McMaster-Carr product ID: 9503K31) with thickness
48 $t_{plate} = 0.075$ mm and Young’s modulus $E = 170$ GPa.
 - 49 – Use an Ultimaker S3 3D printer to fabricate an holder out of PLA material with two slits
50 oriented at an angle $\theta_{plate} = 45^\circ$ with respect to the horizontal direction
 - 51 – Apply an axial force to buckle the rectangular plate into an arch and slide its ends into the
52 two slits of the 3D-printed holder and glue the arch to the slits using ethyl 2-cyanoacrylate
53 glue (Krazy Glue, NC).
 - 54 – 3D print a piston and glue the piston at the center of the arch using Sil-Poxy (Smooth-On).
 - 55 – Cut a segment with length of ~ 40 mm out of a 10 ml plastic syringe with inner diameter
56 of 22 mm. This will form the chamber for the valve.
 - 57 – Cut a dome-shaped notch (with depth around 1 mm and diameter around 5mm) on the
58 internal surface of the cylindrical segment using a rotary tool workstation (220-01 Dremel).
59 When the piston moves across the notch, the on/off state of the valve is changed.
 - 60 – Mount O-rings (Oil-Resistant Soft Buna-N, McMaster-Carr product ID: 2418T138) on the
61 piston and the holder to prevent leaking between the piston (or holder) and the chamber.
 - 62 – Insert the construction of holder, arch and piston into the chamber.
- 63 • *Bistable valve*: The bistable valve is fabricated following the same steps used for the hysteretic
64 valve. The only differences between the two designs are the thickness of the plate (for the
65 bistable valve we use a metallic plate with thickness $t_{plate} = 0.05$ mm) and the mounting angle
66 θ_{plate} (for the bistable valve we use $\theta_{plate} = 0^\circ$).

67 **1.2. Kirigami actuators.** To realize the robotic arm and climbing robot shown in Fig. 2 and 3 of the
68 main text, we use cylindrical kirigami actuators fabricated following the procedure described in our
69 previous work (1) - the only difference is that here we add another thin layer (thickness ~ 1 mm)
70 of Ecoflex 00-50 inside the actuator to enhance its robustness and durability. Specifically, we use
71 three types of actuators which support bending (Actuator I in Fig. S2), extension (Actuator II in
72 Fig. S2) and expansion (Actuator III in Fig. S2). The geometric parameters defining each actuator
73 are shown in Fig. S2 and listed in Table S1. Note that Actuators II and III comprise identical units
74 for the entire structure, whereas to enable bending in Actuator I we introduce one column of unit
75 cells with increased ligament size δ_2 (shown as purple units in Fig. S2).

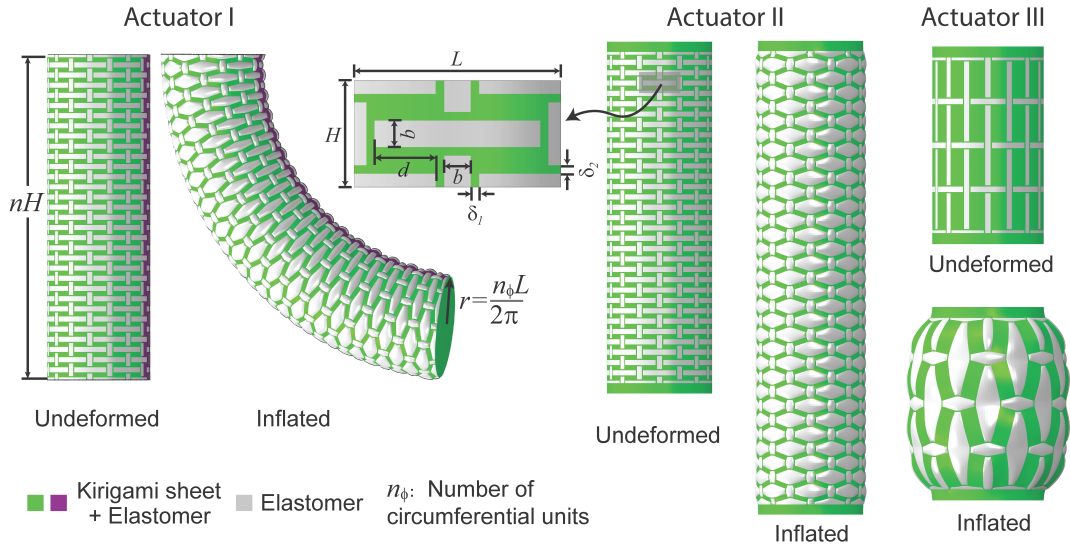


Fig. S2. Kirigami actuators. Three types of kirigami actuators are used in realizing bending (Actuator I), extension (Actuator II) and expansion (Actuator III) deformation. The geometric parameters of the actuators are listed in Table S1.

Geometric parameters defining the actuators							
Geometric parameters	L [mm]	H [mm]	b [mm]	δ_1 [mm]	δ_2 [mm]	n	n_ϕ
Actuator I (purple units)	12	6	3	0.36	2.16	16	1
Actuator I (green units)	12	6	3	0.36	0.36	16	7
Actuator II	12	6	3	0.36	0.36	16	8
Actuator III	12	24	3	0.36	0.36	2	8

Table S1. Geometric parameters defining our kirigami actuators. All parameters are defined in Fig. S2.

76 **1.3. Robotic arm.** The robotic arm is constructed by connecting two bending kirigami actuators
77 (Actuator I in Table S1 and Fig. S2) through a viscous valve or a one-way viscous valve. Specifically,
78 we fabricate the robotic arm using the following steps:

- 79 • Fabricate two identical kirigami actuators (Actuator I in Table S1 and Fig. S2) following the
80 procedure described in our previous work (1). The only difference is that here we add another
81 thin layer (thickness $t \sim 1$ mm) of Ecoflex 00-50 inside the actuator to enhance its robustness
82 and durability. More specifically, we pour additional Ecoflex inside the kirigami actuator and
83 rotate it slowly to achieve a uniform coating.
- 84 • Glue perforated acrylic plates at the ends of the actuator to facilitate connection with other
85 actuators (see Fig. S3). Further, we 3D print a mold to cast elastomeric layers with thickness
86 ~ 1 mm and the same shape as the acrylic plates. Such elastomeric layers are placed between
87 the acrylic plates and the valves to avoid leakages (see Fig. S3).
- 88 • Arrange the two identical bending actuators so that the columns of unit cells with increased
89 ligament size δ_2 are diametrically opposed (Fig. S3).
- 90 • Introduce a viscous valve (or one-way viscous valve) between the two actuators to regulate the
91 flow between them (as shown in Fig. S3). Secure the connection between the actuators and
92 the valve by threading a screw through the acrylic plates and the hole places in the center of
93 the valve.
- 94 • Connect a tube to the top actuator to provide the pressure input.

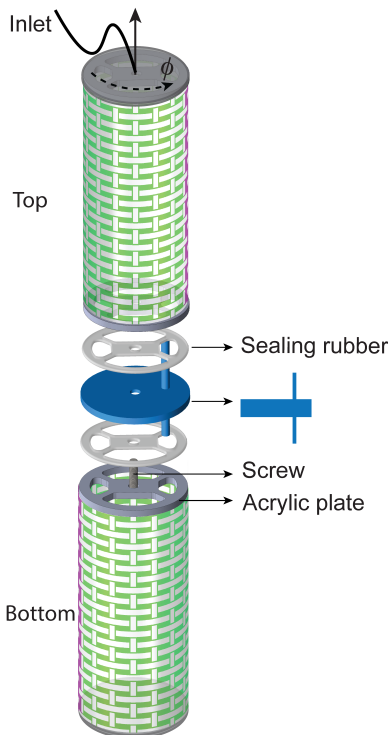


Fig. S3. Schematic of the robotic arm. The robotic arm is constructed by connecting two bending kirigami actuators (Actuator I in Table S1 and Fig. S2) separated by a viscous valve or one-way viscous valve.

95 **1.4. Tube climbing robot.** As shown in Fig. S4A our climbing robot comprises two expanding
96 kirigami actuators (Actuator III in Table S1) and an extending one (Actuator II in Table S1)
97 connected via a one-way viscous valve and a viscous valve. Further, to enable grasping, a hysteretic
98 valve and a gripper consisting of two PneuNets (2) is added at the top (Fig. S4B). To fabricate the
99 robot, we follow the steps below:

- 100 • Fabricate two identical expanding kirigami actuators (Actuator III in Table S1 and Fig. S2)
101 and one extending actuator (Actuator II in Table S1 and Fig. S2) following the procedure
102 described in our previous work (1). The only difference is that here we add another thin
103 layer (thickness $t \sim 1$ mm) of Ecoflex 00-50 inside the actuator to enhance its robustness and
104 durability. More specifically, we pour additional Ecoflex inside the kirigami actuator and rotate
105 it slowly to achieve a uniform coating.
- 106 • Glue perforated acrylic plates at the ends of the actuators to facilitate connection with other
107 actuators (see Fig. S4A). Further, we 3D print a mold to cast elastomeric layers with thickness
108 ~ 1 mm and the same shape as the acrylic plates. Such elastomeric layers are placed between
109 the acrylic plates and the valves to avoid leakages (see Fig. S4A).
- 110 • Introduce a viscous valve between the top extending actuator and the elongating one and
111 a one-way viscous valve between the bottom extending actuator and the elongating one (as
112 shown in Fig. S4). Secure the connection between the actuators and the valve by threading a
113 screw through the acrylic plates and a hole places in the center of the valve.
- 114 • Connect a tube to the bottom actuator to provide the pressure input.

115 Additionally, to realize a robot capable of grasping an object, the following steps are also needed:

- 116 • 3D print the two-part mold shown in Fig. S5A. This mold enables casting of PneuNets with
117 length $l_{gripper} = 30$ mm, width $w_{gripper} = 10$ mm and thickness $t_{gripper} = 5$ mm.
- 118 • Prepare Ecoflex 00-30 and Ecoflex 00-50 to cast the PneuNets.
- 119 • Pour Ecoflex 00-30 inside the main body mold; pour Ecoflex 00-50 inside the base mold up to
120 $2/3$ of its height (~ 2 mm, Fig. S5B).
- 121 • Cure the Ecoflex for about an hour at room temperature.
- 122 • Remove the cured Ecoflex 00-30 from the main mold
- 123 • Apply a layer (with thickness of ~ 0.5 mm) of uncured Ecoflex 00-50 on top of the cured
124 Ecoflex 00-50 (while keeping the part in the base mold)
- 125 • Slowly place the Ecoflex 00-30 structure obtained from the main mold on top of the base mold.
126 The uncured Ecoflex 00-50 enables bonding between the two pieces.
- 127 • Remove the soft actuator from the mold.
- 128 • Insert a short tube in one end of the PneuNets.
- 129 • Laser cut a circular acrylic plate with diameter of 30 mm and thickness of 1/16 inch.

- 130 • Cut three holes (with diameter of 3 mm) in the acrylic plate: (a) the one at the center is used
131 for the connection with the top actuator via a screw; and (b) the other two holes, located at
132 the margin of the plate, are used to pass through the short tubes that connect to the PneuNets.
- 133 • Apply glue (Sil-Poxy Silicone Adhesive, Smooth-On) to secure the tube and PneuNets to the
134 acrylic plate.
- 135 • Attach a hysteretic valve to the top expanding actuator and connect the gripper to its chamber.
136 Apply glue (Sil-Poxy Silicone Adhesive, Smooth-On) to fix and seal the valve and the gripper.
- 137 • The robot is ready to be tested.

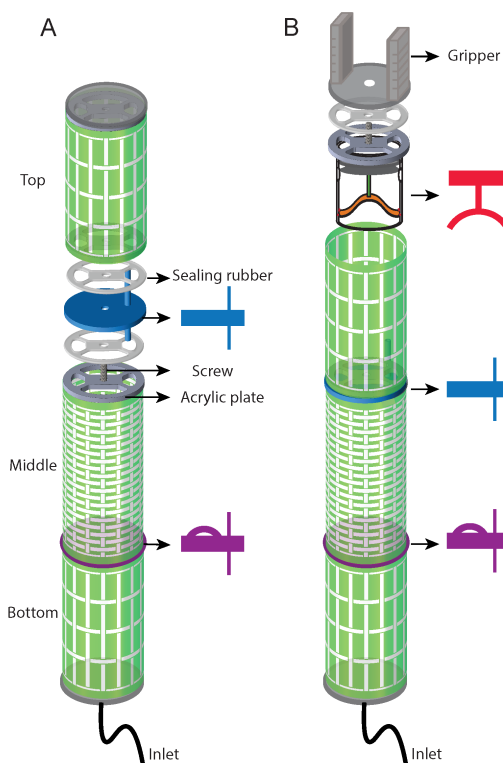


Fig. S4. Schematic of the climbing robot. (A) The climbing robot comprises two expanding kirigami actuators (Actuator III in Table S1) and an extending one (Actuator II in Table S1) connected via a one-way viscous valve and a viscous valve. (B) A hysteretic valve and a gripper consisting of two PneuNets (2) is added to the top actuator to enable grasping.

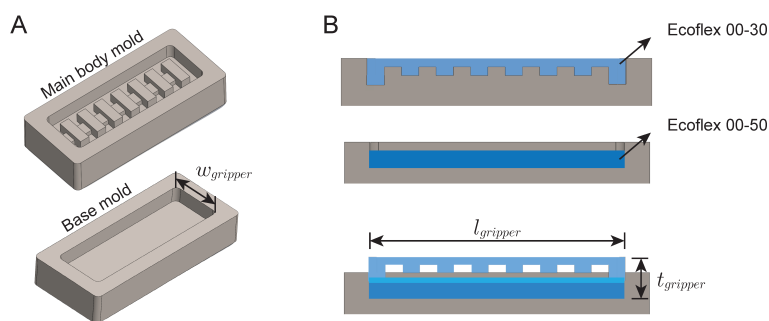


Fig. S5. Fabrication of the gripper. (A) 3D printed molds for the gripper. (B) Fabrication procedure.

138 **1.5. Rolling robot.** The rolling robot demonstrated in this study is made of nearly incompressible
139 silicon rubbers. Specifically, we use Elite Double 32 (with green color and initial shear modulus
140 $\mu = 0.35$ MPa, Zhermack) for the hexagonal frame of the robot and Ecoflex 00-50 (with white
141 translucent color and initial shear modulus $\mu = 0.0405$ MPa, Smooth-On, PA) for the deformable
142 chambers. 12 chambers are evenly distributed along the perimeter of the robot (two on each side),
143 which are connected to the pressure source via six viscous valves and a modified bistable valve. The
144 robot is fabricated using a molding approach according to the following 8 steps (Fig. S6):

- 145 • **Step A-1:** 3D print the mold shown in Fig. S6A using PLA material with a Ultimaker S3
146 printer. We insert screws inside the mold to facilitate the connection of the tubes in *Step G*.
- 147 • **Step A-2:** pour Ecoflex 00-50 into the mold to cast the skeleton of the chambers and let it
148 cure for 30 minutes at room temperature. Note that the height of the Ecoflex should not be
149 higher than that of the mold's islands shown in Fig. S6A.
- 150 • **Step B:** pour Elite Double 32 into the mold (on top of the cured Ecoflex 00-50) to cast one
151 side of the frame.
- 152 • **Step C:** wait for Elite Double 32 to cure for 30 minutes.
- 153 • **Step D:** remove the cured Ecoflex 00-50 and Elite Double 32 from the mold. Note that this
154 two materials bond naturally.
- 155 • **Step E:** use another mold to cast the other hexagonal frame of the robot, pour Elite Double
156 32 into the mold until the thickness is about 4/5 of the mold's thickness.
- 157 • **Step F:** when the Elite Double 32 frame is half cured (after ~ 15 minutes), pour more Elite
158 Double 32 onto the half cured skeleton (to reach the full thickness) and then place the structure
159 from *Step d* on top of it to seal the frame and the chambers.
- 160 • **Step G:** connect two sets of tubes to the robot to form two circuits. Each set has six tubes
161 attached to the six chambers (one at each side of the robot). Three tubes in each set are
162 equipped with a viscous valve. Note that to facilitate the (dis)assembling of the valves from the
163 robot, we split each tube into two segments and attach them using a luer lock (with internal
164 diameter 1/8 inch). We then insert the viscous valves into the luer lock. Note that in this
165 case, we glue and seal the narrow needle (with length $l_{tube} = 25$ mm and diameter $d_{tube} = 0.26$
166 mm) of the viscous valve directly into the luer lock using Sil-poxy).
- 167 • **Step H:** Connect the two sets of tubes via a bistable valve (see the connection in Fig. S7).
- 168 • Modify the design of the bistable valve to enable bi-directional rolling. More specifically, we
169 replace the notch with a hole with diameter of 1.6 mm. When the input source is connected
170 to this hole (Fig. S7A), the new version of the bistable valve is able to switch the flow from
171 one circuit to the other. This is possible by applying a negative pressure burst to the input to
172 change the position of the piston and snap the arch at the same time, which forces the piston
173 to stay in the new position. The connection between the bistable valve and viscous valves is
174 shown in Fig. S7B.
- 175 • Add additional acrylic rods to one face of the robot to stabilize it and prevent it to fall sideways
176 during the test (see Fig. 4D in main text).

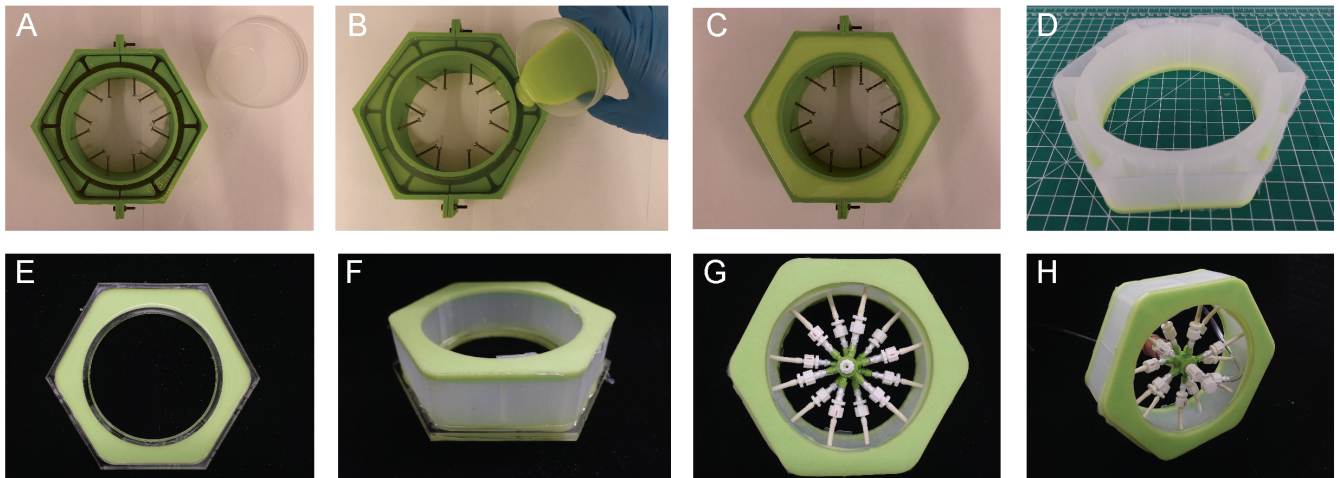


Fig. S6. Fabrication of the rolling robot. Snapshots of the 8 steps required to fabricate the robot.

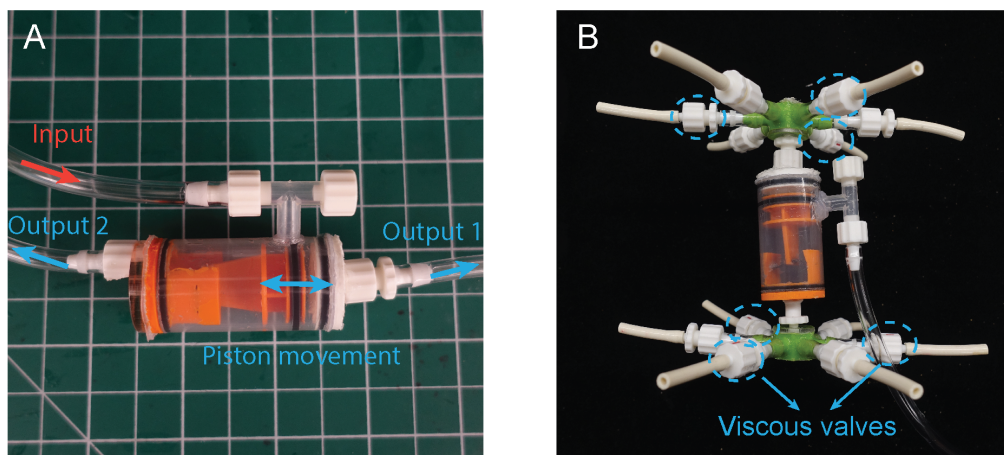


Fig. S7. Connection of the valves for rolling robot. (A) Working principle of the modified bistable valve. By changing the position of the piston, we can switch the flow from one circuit to the other. (B) The connection between the bistable valve and the two circuits.

177 **2. Experiments**

178 In order to characterize the effect of the valves on the response of the robotic systems, we use
179 pressurized air of the order of a few kPa. To achieve such levels of pressure, we decrease the pressure
180 from the wall air-outlet (~ 200 psi) using two pressure regulators (B74G-4AK-AD3-RMN by IMI
181 Norgren Inc and ITV1030 by SMC Cooperation). The first pressure regulator reduces the inlet
182 pressure from 200 psi to about ~ 200 kPa, while the second one accurately controls the pressure
183 in the range $[0, 200]$ kPa. Further, to turn on and off the input pressure we used a standard
184 two-way solenoid valves (KVE32PL24FF by Kamoer) to switch on/off the inlet of the system to the
185 atmosphere, so that the actuators could deflate and return to their initial state.

186 **2.1. Characterization of the mechanical valves.** To characterize all our mechanical valves, we
187 connect each of them to an extension actuator (Actuator II in Table S1) and monitor the pressure
188 evolution both at the inlet and inside the actuator using two pressure sensors (MPXV7025DP,
189 Freescale Semiconductor Inc - Fig. S8). During the tests the deformation of the actuator is also
190 recorded by a high-resolution camera (SONY EX100V) at a frame rate of 30 fps. The recorded
191 input/output pressure evolution for each valve is reported in Fig. 1 of the main text.

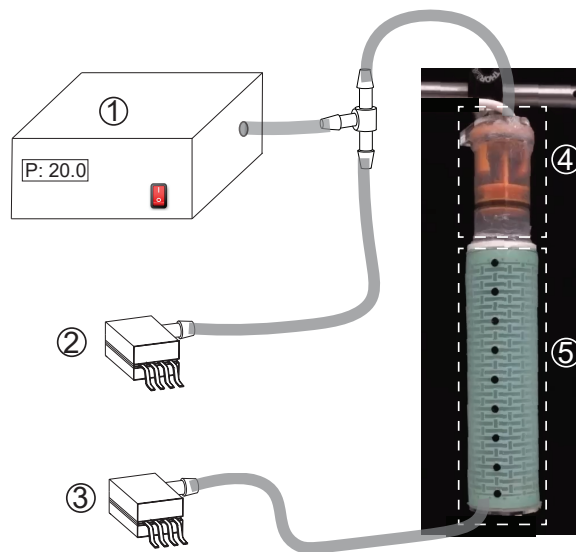


Fig. S8. Characterization of the mechanical valves. Schematic of the test setup used to characterize the valves. (1) Pressure control system. (2) Pressure sensor for the inlet. (3) Pressure sensor for the actuator. (4) Mechanical valve. (5) Actuator.

192 **2.2. Characterization of the kirigami actuators.** As part of this study we also experimentally
193 characterize the pressure-volume evolution of each kirigami actuator using the setup shown in Fig.
194 S9A. To decouple the effect of the geometry of the actuators from that of the compressibility of
195 the fluid, we determine the pressure-volume curve by inflating the actuators with water. Further,
196 to eliminate the influence of gravity, we submerge the entire actuator in a water tank. In all our
197 tests, we first fill the actuator with the amount of water corresponding to the initial volume of the
198 cavity. Then, we use a syringe pump (Pump 33DS, Harvard Apparatus) to displace an additional
199 volume of water ΔV into the balloons at 20 mL/min (ensuring quasi-static conditions) and record
200 the pressure using a pressure sensor (MPXV7025DP, Freescale Semiconductor Inc). Since as part
201 of this study we use the kirigami actuators in an unconstrained environment for the robotic arm

202 and constrained within a tube for the climbing robot, we test them both in unconstrained and
 203 constrained conditions. More specifically, we test Actuator I and II under unconstrained conditions
 204 and find a liner dependence of the pressure from the supplied volume (Fig. S9B). Further, we test
 205 Actuator II and III when placed in a tube with diameter of 35 mm (identical to the tube used to test
 206 the climbing robot). As shown in Fig. S9C, in this case we find a highly non-linear pressure-volume
 207 curve, as the pressure abruptly increases when the actuators get in contact with the tube.

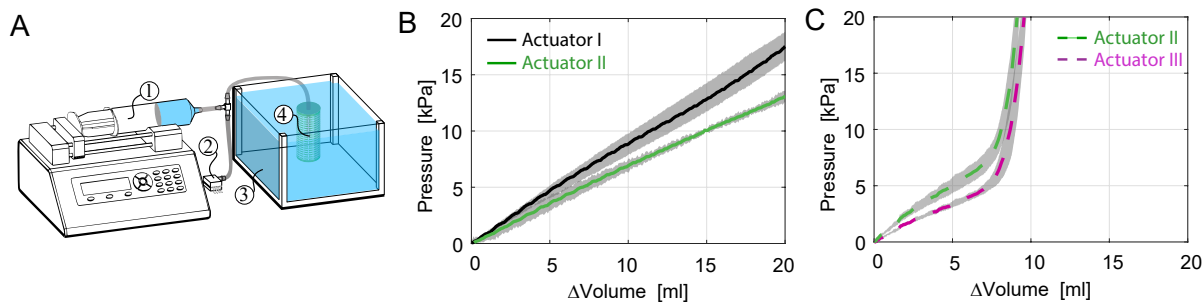


Fig. S9. Pressure-volume characterization of the kirigami actuators. (A) Schematic of the test setup used to characterize the pressure-volume relations of actuators. (1) Syringe pump. (2) Pressure sensor. (3) Water tank. (4) Actuator. (B) Pressure-volume relations recorded for Actuators I and II when tested in unconstrained conditions. (C) Pressure-volume relations recorded for Actuators II and III when tested in constrained conditions.

208 **2.3. Robotic Arm.** To characterize the deformation of our robotic arm, we monitor with a high-
209 resolution camera (SONY RX100V) recording at a frame rate of 30 fps (i) 17 black circular markers
210 uniformly placed along the length of the kirigami actuators and (ii) a white circular marker placed
211 at the end of an acrylic rod connected to the bottom cap. We extract the coordinates of all markers
212 using an open-source digital image correlation and tracking package (3). We then use the coordinates
213 of the white marker to determine the trajectory followed by the robotic arm. Further, we determine
214 the radius R of the circle that best fits the black markers via a direct least-square algorithm (4, 5)
215 and calculate the average curvature of the two actuators as

$$216 \quad \kappa = 1/R. \quad [S1]$$

217 Finally, we note that during the tests the evolution of the pressure inside the actuators is monitored
218 by pressure sensors (MPXV7025DP, Freescale Semiconductor Inc).

219 In Figs. S16 and S17 we consider the robotic arm with a viscous valve and one-way viscous
220 valve, respectively, and report the recorded tip trajectory (left), pressure evolution in both actuators
221 (middle) and curvature evolution of both actuators (right) for different pressure inputs.

222 **2.4. Tube climbing robot.** To test the climbing robot, we place the system inside a vertically oriented
223 acrylic tube with inner diameter of 35 mm and supply many pressure pulses, while recording its
224 motion using a high-resolution camera (SONY RX100V).

225 Further, we conduct additional tests to characterize both the frictional force between the expanding
226 actuator and the tube and the axial force exerted by the extending actuator interaction between the
227 robot and the tube, as well as the extension force generate by the extending actuator.

228 As shown in Fig. S10A, to characterize the frictional force, we place an expanding actuator inside
229 a vertically oriented acrylic tube (with inner diameter of 35 mm) and connect it to a motorized
230 translation stage (LTS300/M , ThorLabs) via a nylon thread. During our tests, we inflate the
231 actuator by supplying different amount of pressure (0 – 6 kPa) and pull the actuator upward using
232 the linear stage with speed of 0.2 mm/s. The friction force between the tube and actuator is
233 measured using a 10 lb load cell (LSB200 Miniature S-Beam Jr. Load cell, FUTEK Advanced Sensor
234 Technology, Inc.). The recorded evolution of the friction as a function of applied pressure is reported
235 in Fig. 3C of the main text.

236 To measure the axial force generated by the extending actuator, we use the same setup as that
237 use to measure the frictional force except that we use screws to connect the load cell to the linear
238 stage and the actuator(Fig. S10B). During our tests, we fix the movement of the linear stage and
239 increase the pressure inside the actuator gradually and record the axial force as a function of the
240 pressure using the load cell. The recorded evolution of the force as a function of applied pressure is
241 reported in Fig. 3C of the main text.

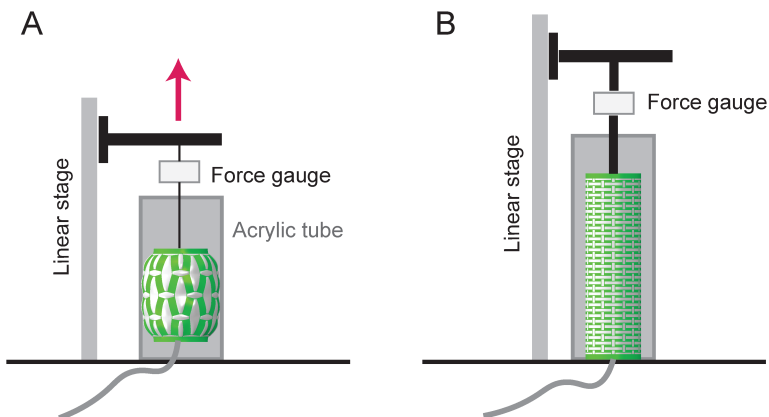


Fig. S10. Schematics of the experimental setups used to measure frictional and extension forces. (A) Setup for measuring friction. (B) Setup for measuring extension force.

242 **2.5. Rolling robot.** To actuate our rolling robot we connect it to our pressure control system (Fig.
243 S8) and supply the pressure profile shown in Fig. S11. Note that the input pressure for each cycle
244 consists of 2 pressure pulses:

- 245 • *Pulse 1:* the first pressure pulse ($p_{input} = 15$ kPa for $t_{input} = 3$ s) is provided to rapidly inflate
246 the chambers connected directly to the pressure supplier (snapshot 2 in Fig. 4C of main text).
247 This high pressure pulse accelerate the inflation of the chambers connected directly to the
248 pressure source but has negligible effect on the chambers attached to the viscous valves.
- 249 • *Pulse 2:* a moderate pressure pulse ($p_{input} = 10$ kPa for $t_{input} = 67$ s) then follows the high
250 pressure pulse to gradually inflate the chambers attached to the viscous valves. Note that after
251 supplying this second pulse all chambers are inflated (snapshot 4 in Fig. 4C of main text).

252 When the input pressure is removed, the chambers with no viscous valve deflate instantaneously,
253 while the ones with viscous valves keep the inflated state temporarily and push the robot to rotate
254 further (snapshot 5 in Fig. 4C of main text).

255 To change the rolling direction of the robot we apply a negative pressure burst with magnitude
256 large enough (~ 25 kPa) to change the position of the piston and snap the arch at the same time.

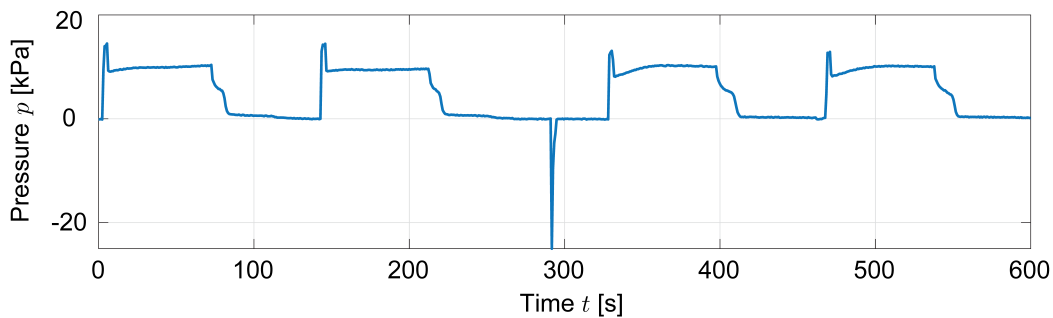


Fig. S11. Pressure supplied to the rolling robot for bidirectional locomotion.

257 3. Modeling

258 To get a better understanding of the behavior of the proposed valves, we use numerical analyses.
 259 For the viscous valves, we simplify the Navier–Stokes equations to calculate the pressure drop. For
 260 the hysteretic and bistable valves, we conduct Finite Element (FE) simulations to characterize the
 261 mechanical response of the arches.

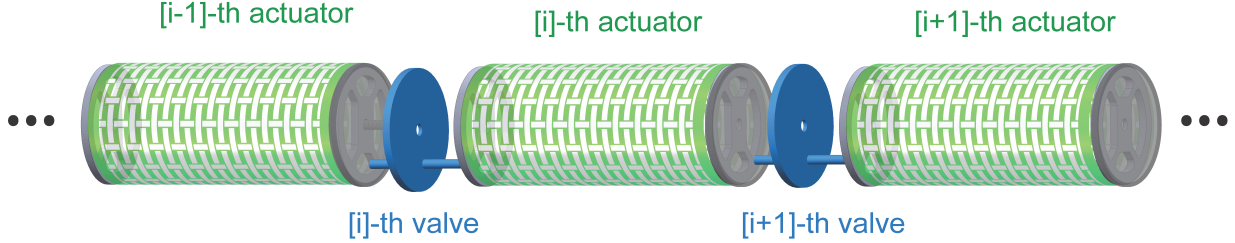


Fig. S12. Schematic of the model for the viscous valves.

262 **3.1. Viscous valves.** Our viscous valves comprise narrow tubes to provide a transient pressure
 263 difference between adjacent actuators. To predict their response, we use a numerical model recently
 264 proposed by Vasios et al (6). More specifically, we focus on the $[i]$ -th valve in the actuator that
 265 comprises a narrow tube of length $l_{tube,i}$ and diameter $d_{tube,i}$ and assume that

- 266 • the tube is rigid and not deformed by the flow;
- 267 • the head losses due to friction at the connections between the tube and the actuators can be
 268 captured by adjusting its length to $l_{tube,i}^{eq}$;
- 269 • the flow is incompressible and laminar in the narrow tube;
- 270 • the fluid velocity has the form

$$271 \quad \mathbf{u} = -\frac{8}{\pi d_{tube,i}^2} \frac{d\tilde{v}_i}{dt} \left[\left(\frac{r}{R_i} \right)^2 - 1 \right] \mathbf{e}_z, \quad [\text{S2}]$$

272 where $\tilde{v}_i = \int_0^t \int_0^{d_{tube,i}/2} \mathbf{u} \cdot \mathbf{e}_z 2\pi r dr dt$ denotes the amount of fluid exchanged through the $[i]$ -th
 273 tube up to time t and \mathbf{e}_z identifies the tangent vector to the tube;

- 274 • the inertia term is negligible, since the tubes are narrow ($l_{tube,i} \gg d_{tube,i}$).

275 Under these assumptions, integration of the Navier–Stokes equations over the volume of the tube
 276 yields

$$277 \quad \frac{d\tilde{V}_i}{dT} + \xi_i (P_i - P_{i-1}) = 0, \quad \text{for } i = 1, \dots, N \quad [\text{S3}]$$

278 with

$$279 \quad \xi_i = \frac{\pi G d_{tube,i}^4 t_{max}}{128 \mu v_0 l_{tube,i}^{eq}}, \quad [\text{S4}]$$

280 where $\tilde{V}_i = \tilde{v}_i / v_0$ is the normalized volumetric flow through the $[i]$ -th tube (v_0 denoting the volume
 281 of the largest actuator in the system), $T = t / t_{max}$ is the normalized time (t_{max} denoting the response

282 time of the system) and $P_i = p_i/G$ is the normalized pressure in the $[i]$ -th actuator (p_i being the
 283 pressure inside the $[i]$ -th actuator and G being the shear modulus of the material used to fabricate
 284 the actuator). Note that $1/\xi_i$ expresses an equivalent resistance that the $[i]$ -th valve imposes to fluid
 285 flow; when ξ_i is large, high flow rates dV_i/dT are achieved for relatively low pressure differences,
 286 whereas when ξ_i is small, the opposite is true.

287 Next, we connect the amount of fluid exchanged through the valves to the amount of fluid present
 288 in the chambers of the actuators. When an incompressible fluid such a water is used to inflate the
 289 system, the normalized change in volume for the $[i]$ -th actuator, $\Delta V_i = \Delta v_i/v_0$, can be expressed in
 290 terms of the volumetric flows exchanged through the two tubes connected to it as

$$291 \quad \Delta V_i = \tilde{V}_i - \tilde{V}_{i+1}. \quad [S5]$$

292 Differently, when, as in this study, we use a compressible fluid (air) to inflate the robotic system,
 293 we focus on the number of moles of fluid exchanged though the valves. Specifically, the change in
 294 number of moles of air for the $[i]$ -th actuator, Δn_i , can be determined as

$$295 \quad \Delta n_i = \tilde{n}_i - \tilde{n}_{i+1}, \quad [S6]$$

296 where \tilde{n}_i denotes the number of moles of air exchanged through the $[i]$ -th valve. Further, the total
 297 number of moles of air in the $[i]$ -th actuator at time T can be expressed as

$$298 \quad n_i(T) = n_i(T=0) + \int_0^T \frac{d\Delta n_i}{dT} dT = n_i(T=0) + \int_0^T \frac{d(\tilde{n}_i - \tilde{n}_{i+1})}{dT} dT. \quad [S7]$$

299 Note that, by introducing the ideal gas law n_i and \tilde{n}_i can be written as

$$300 \quad n_i = \frac{P_i V_i}{R_g \Theta_i}, \quad \tilde{n}_i = \frac{\bar{P}_i \tilde{V}_i}{R_g \bar{\Theta}_i}, \quad [S8]$$

301 where V_i denotes the volume for the $[i]$ -th actuator, R_g is the ideal gas constant and Θ is the
 302 temperature. Moreover,

$$303 \quad \bar{P}_i(T) = \begin{cases} P_{i-1} & \text{for } \frac{d\tilde{V}_i}{dT} \geq 0, \\ P_i & \text{for } \frac{d\tilde{V}_i}{dT} < 0, \end{cases}$$

304 and

$$305 \quad \bar{\Theta}_i(T) = \begin{cases} \Theta_{i-1} & \text{for } \frac{d\tilde{V}_i}{dT} \geq 0, \\ \Theta_i & \text{for } \frac{d\tilde{V}_i}{dT} < 0. \end{cases}$$

306 Note that if the air flows from the $[i-1]$ -th actuator to $[i]$ -th acuator, the pressure and temperature
 307 inside the $[i-1]$ -th actuator should be used to calculate \tilde{n}_i , whereas when the air flows from the
 308 $[i]$ -th actuator to $[i-1]$ -th acuator, \tilde{n}_i is determined based on the pressure and temperature inside
 309 the $[i]$ -th actuator.

310 If we assume the actuation to be an isothermal process (i.e. we assume that the temperature of
 311 the air inside the actuators is constant), substitution of Eqs. (S8) into Eq. (S7) yields

$$312 \quad P_i(T)V_i(T) = P_i(0)V_i(0) + \int_0^T \bar{P}_i(T) \frac{d\tilde{V}_i(T)}{dT} dT - \int_0^T \bar{P}_{i+1}(T) \frac{d\tilde{V}_{i+1}(T)}{dT} dT, \quad [S9]$$

313 where $V_i(0)$ is the initial volume of the $[i]$ -th actuator and $P_i(0)$ is the initial pressure inside the
 314 $[i]$ -th actuator (i.e. atmospheric pressure $P_i(0) = 101.3$ kPa). Finally, by substituting Eq. (S3) into

Eq. (S9), we obtain

$$P_i(T)V_i(T) = P_i(0)V_i(0) - \int_0^T \xi_i \bar{P}_i(T) [P_i(T) - P_{i-1}(T)] dT + \int_0^T \xi_{i+1} [\bar{P}_{i+1}(T)(P_{i+1}(T) - P_i(T))] dT, \quad [\text{S10}]$$

For a system comprising N fluidic actuators interconnected via viscous valves Eq. (S10) results in a system of N coupled differential equations, which given a pressure-volume relationship for the actuators that can be numerically solved to determine the normalized change in volume for the $[i]$ -th actuator as a function of time. Finally, we note that for the first and last tube in the array Eq. (S10) needs to be modified as

$$P_1(T)V_1(T) = P_1(0)V_1(0) - \int_0^T \xi_1 \bar{P}_1(T) [P_1(T) - P_{input}(T)] dT + \int_0^T \xi_2 [\bar{P}_2(T)(P_2(T) - P_1(T))] dT, \quad [\text{S11}]$$

and

$$P_N(T)V_N(T) = P_N(0)V_N(0) - \int_0^T \xi_N \bar{P}_N(T) [P_N(T) - P_{N-1}(T)] dT, \quad [\text{S12}]$$

to account for the pressure input and the end of the array.

Individual valves. For the simple setup considered in Fig. 1D of the main text (comprising a rigid chamber and an extension kirigami actuator separated by a viscous valve), Eq. (S10) specializes to

$$P(T)V(T) = P(0)V(0) - \int_0^T \xi \bar{P}(T)(P(T) - P_{input}(T)) dT, \quad [\text{S13}]$$

where P and \tilde{V} denote the volume and pressure of the actuator and $P_{input}(t)$ is the normalized input pressure supplied to the rigid chamber

$$P_{input}(T) = \begin{cases} p_{input}/G & \text{for } T \leq T_{input}, \\ 0 & \text{for } T > T_{input}. \end{cases} \quad [\text{S14}]$$

Note P and V are not independent, as they follow the experimentally measured pressure-volume relationship shown in Fig. S9. To estimate ξ for a given valve we compare the time evolution of pressure measured in our experiments with the numerical prediction obtained by numerically solving Eq. (S13) with the pressure-volume relationship reported in Fig. S9B (Actuator II). We find excellent agreement between experimental results and numerical predictions when choosing (see Fig. S13)

- $\xi = 14.2$ for a viscous valve with $d_{tube} = 0.21$ mm;
- $\xi = 14.2$ for a one-way viscous valve with $d_{tube} = 0.21$ mm and flow in the forward direction
- $\xi = 716.2$ for a one-way viscous valve with $d_{tube} = 0.21$ mm and flow in the backward direction

Note that these values for ξ are also summarized in Table S2.

Robotic arm. For the robotic arm considered in Fig. 2 of the main text (which comprises two bending kirigami actuators connected through a viscous valve with $d_{tube} = 0.21$ mm), Eq. (S10) specializes to

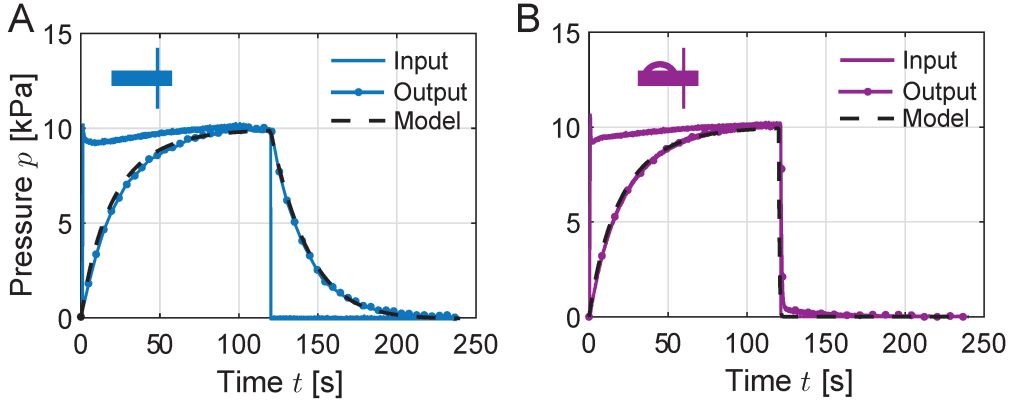


Fig. S13. Model vs. experiments. (A) Comparison between experimental results (blue line) and model predictions (black line) for a viscous valve with tube length $l_{tube} = 25$ mm and internal diameter $d_{tube} = 0.21$ mm. (B) Comparison between experimental results (purple line) and model predictions (black line) for a one-way viscous valve with tube length $l_{tube} = 25$ mm and internal diameter $d_{tube} = 0.21$ mm. The equivalent conductance use in the mechanical valves are reported in Table S2.

	Viscous valve ($d_{tube} = 0.21$ mm)	One-way viscous valve ($d_{tube} = 0.21$ mm) [forward direction]	One-way viscous valve ($d_{tube} = 0.21$ mm) [backward direction]
ξ_i	14.2	14.2	716.2

Table S2. Equivalent conductance of the viscous valves.

$$\begin{cases} P_1(T)V_1(T) = P_1(0)V_1(0) - \int_0^T \xi_1 \bar{P}_1(T)(P_1(T) - P_{input}(T))dT + \int_0^T \xi_2 \bar{P}_2(T)(P_2(T) - P_1(T))dT, \\ P_2(T)V_2(T) = P_2(0)V_2(0) - \int_0^T \xi_2 \bar{P}_2(T)(P_2(T) - P_1(T))dT, \end{cases} \quad [S15]$$

345

346 where the subscripts 1 and 2 refer to the top and bottom actuator, respectively. Further, ξ_1 and
 347 ξ_2 denote the equivalent resistance encountered by the fluid between the input source and the top
 348 actuator and the equivalent resistance imposed by the viscous valve, respectively. Note that the
 349 values for ξ_2 are reported in Table S2, whereas for the connection between the input source and the
 350 first actuator we use $\xi_1 = 472.7$. Finally, to connect P and V , we use the experimentally measured
 351 pressure-volume relationship shown in Fig. S9B (Actuator I). As shown, in Figs. S16 and S17 the
 352 model nicely capture the response of the arm with both a viscous and one-way viscous valve for a
 353 wide range of pressure inputs.

354 **Climbing robot.** For the climbing robot considered in Fig. 3 of the main text (which comprises
 355 three bending kirigami actuators connected through a viscous valve with $d_{tube} = 0.21$ mm and a
 356 one-way viscous valve with $d_{tube} = 0.21$ mm), Eq. (S10) specializes to

$$\begin{cases} P_1(T)V_1(T) = P_1(0)V_1(0) - \int_0^T \xi_1 \bar{P}_1(T)(P_1(T) - P_{input}(T))dT + \int_0^T \xi_2 \bar{P}_2(T)(P_2(T) - P_1(T))dT, \\ P_2(T)V_2(T) = P_2(0)V_2(0) - \int_0^T \xi_2 \bar{P}_2(T)(P_2(T) - P_1(T))dT + \int_0^T \xi_3 \bar{P}_3(T)(P_3(T) - P_2(T))dT, \\ P_3(T)V_3(T) = P_3(0)V_3(0) - \int_0^T \xi_3 \bar{P}_3(T)(P_3(T) - P_2(T))dT, \end{cases} \quad [S16]$$

357

358 where the subscripts 1, 2 and 3 refer to the bottom, middle and top actuators. Further, ξ_1 is the
 359 equivalent resistance between the input source and the bottom actuator, ξ_2 denotes the equivalent
 360 resistances of the one-way viscous valve and ξ_3 represent the equivalent resistances of the viscous
 361 valve. Note that the values for ξ_2 and ξ_3 are reported in Table S2, whereas for the connection

362 between the input source and the first actuator we use $\xi_1 = 472.7$. Finally, to connect P and V ,
 363 we use the experimentally measured pressure-volume relationship shown in Fig. S9C. As shown in
 364 Fig. S20, we find that the model (dashed lines) agree well with the experimental measurements
 365 (solid lines) for all considered pressure inputs.

366 **3.2. Snapping arch.** To identify the geometric features resulting either in a snapping or in a
 367 bistable arch, we perform Finite Element (FE) analyses using the commercial package ABAQUS
 368 2019/Standard. In our analyses we consider plates with width $w_{plate} = 5$ mm, length $l_{plate} \in [17, 19.5]$
 369 mm, thickness t_{plate} equal to either 0.05 mm or 0.075 mm and mounting angle $\theta_{plate} \in [0^\circ, 60^\circ]$. We
 370 discretize the plate using four-node general-purpose shell elements with reduced integration and
 371 hourglass control (S4R element type). Further, since plasticity has little effect on the observed
 372 phenomena, we capture the material behavior using a linear elastic material model (with Young's
 373 modulus $E = 170$ GPa and Poisson's ratio $\nu = 0.3$). We then simulate the response of the arch
 374 conducting non-linear static simulations under displacement control and dynamic implicit simulations
 375 under load control. The simulations consist of two steps

- 376 • **Step 1:** We buckle a flat plate to an arch by applying an in-plane compression displacement
 377 $d_{in} = (l_{plate} - w)/2$ ($w = 16$ mm being the distance between the two slits of the holder - Fig.
 378 S14B) and a rotation angle θ_{plate} to both end of the arch.
- 379 • **Step 2:** We fix the displacement and rotation at both ends of the arch. For displacement
 380 control simulations we apply an out-of-plane displacement d_{out} at the center of the arch (see
 381 Fig. S14A)) and record the reaction force F . For the load control simulations, we apply a
 382 force F at the center of the arch (see Fig. S14B) and record the displacement d_{out} . Note that
 383 the force F can be expressed as a function of the applied pressure as

$$F = p\pi r^2, \quad [S17]$$

384 where r is the radius of the chamber.

385 In Fig. S14C, we report the numerically predicted evolution of the equivalent pressure p as a
 386 function of the out-of-plane displacement d_{out} for an arch with $\theta_{plate} = 45^\circ$, $l_{plate} = 17.5$ mm and
 387 $t_{plate} = 0.075$ mm. The continuous line represents the FE results of the arch under displacement
 388 control (by applying a displacement d_{out} at the center of the arch). The non-monotonic behavior of
 389 the arch is clearly visible. However, in our mechanical valves the flow pressurizes the piston, which
 390 transfers the force to the central point of the arch. Hence, the boundary conditions of the experiments
 391 are different from those of the simulations under displacement control. To quantify the effect of such
 392 boundary conditions, we also report the response obtained from our load control simulations (black
 393 dashed curves in Fig. S14C). In this case we can see that the pressure-displacement relation of the
 394 arch exhibits a linear regime at the beginning of the loading step. Then, as the pressure increases to
 395 a certain value p_{on}^* , the central point of the arch jumps from positions I to II (characterized by a
 396 plateau on the curve) and, in turn, changes the position of the piston and switches on the valve.
 397 Furthermore, when we reduce the pressure, the arch can snap back at pressure p_{off}^* from positions
 398 III to IV and switch off the valve.

399 It is worth noticing that the model results have to be corrected by taking into account the
 400 contribution of the friction force between the piston and the chamber. We measure this force to
 401 be $F_{friction} = 2.2$ N and always opposed to the moving direction of the piston. Therefore the real

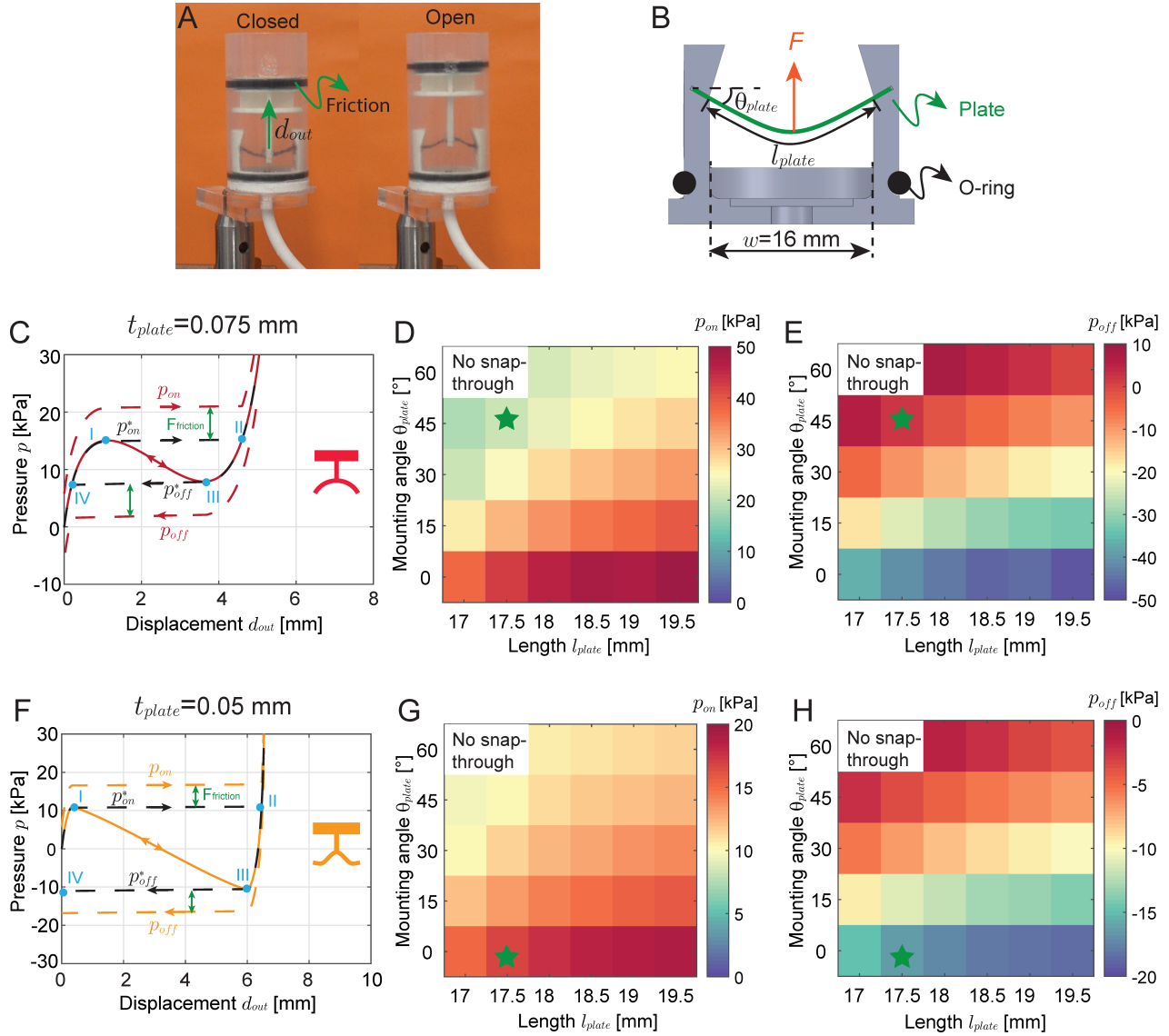


Fig. S14. FE simulations for the hysteretic and bistable valves. (A) Experimental snapshots of a bistable valve in the closed and open states. (B) Schematic of a 3D printed holder for the plate. The mechanical behavior of the valve can be tuned by changing the mounting angle (θ_{plate}), length (l_{plate}) and thickness (t_{plate}) of the plate (we fix the width of the plate $w_{plate} = 5$ mm throughout this study). (C) Mechanical response of an hysteretic valve with $\theta_{plate} = 45^\circ$, $l_{plate} = 17.5$ mm and $t_{plate} = 0.075$ mm. Continuous red line and black dashed lines represent the FE results of the plate under displacement control and force control, respectively. Red dashed lines represent the behavior of the valve with consideration of the friction between the piston and the chamber. The on/off pressures of the valve are $p_{on} = 20.8$ kPa and $p_{off} = 2.1$ kPa, respectively. (D,E) Phase diagrams of (D) p_{on} and (E) p_{off} for a valve with $t_{plate} = 0.075$ mm as a function of θ_{plate} and l_{plate} . (F) Mechanical response of a bistable valve with $\theta_{plate} = 0^\circ$, $l_{plate} = 17.5$ mm and $t_{plate} = 0.05$ mm. Continuous orange line and black dashed lines represent the FE results of the plate under displacement control and force control, respectively. Orange dashed lines represent the behavior of the valve with consideration of the friction between the piston and the chamber. The on/off pressures of the valve are $p_{on} = 16.3$ kPa and $p_{off} = -16.3$ kPa, respectively. (G,H) Phase diagrams of (G) p_{on} and (H) p_{off} for a valve with $t_{plate} = 0.05$ mm as a function of θ_{plate} and l_{plate} .

402 response of the valve can be obtained by shifting the black dashed line up (for the loading curve) or
 403 down (for the unloading curve) by the amount of the equivalent pressure generated by the friction
 404 force (see red dashed lines in Fig. S14C). As a result, the corrected on/off pressure of the valve reads

$$p_{on} = p_{on}^* + \frac{F_{friction}}{\pi r^2}, \quad p_{off} = p_{off}^* - \frac{F_{friction}}{\pi r^2}. \quad [S18]$$

405 In order to design a valve with a prescribed on/off pressure, in Figs. S14D and E we report the
 406 phase diagrams of p_{on} and p_{off} for a valve with $t_{plate} = 0.075$ mm as a function of the mounting

407 angle θ_{plate} and length l_{plate} . Instructed by the model, we choose $\theta_{plate} = 45^\circ$ and $l_{plate} = 17.5$ mm as
 408 design parameters, which enables the on/off switch of the valve at 20.8 kPa and 2.1 kPa, respectively.

409 For the bistable valve, we reduce the thickness of the plate to $t_{plate} = 0.05$ mm in order to operate
 410 the valve at around 20 kPa. Similarly, we report the response of the bistable valve (with $\theta_{plate} = 0^\circ$
 411 and $l_{plate} = 17.5$ mm) in Fig. S14F and the phase diagrams for p_{on} and p_{off} for a valve with
 412 thickness $t_{plate} = 0.05$ mm in Figs. S14G and H, respectively. For the rolling robot, we choose
 413 $\theta_{plate} = 0^\circ$ and $l_{plate} = 17.5$ mm as design parameters of the bistable valve, which enable the on/off
 414 switch of the valve at 16.3 kPa and -16.3 kPa, respectively.

415 Please note that under load control the simulation of the snapping arch beyond point I or III
 416 often incurs in convergence problems (Fig. S14C), providing incomplete information about the
 417 response of the arch. However, the local maximum and minimum pressures for the displacement
 418 control curves are identical to those for the load control curves. Therefore the p_{on}^* and p_{off}^* values
 419 can be extracted from the displacement control simulations. In turn, we can calculate p_{on} and p_{off}
 420 for the phase diagrams by correcting these results to take into account friction.

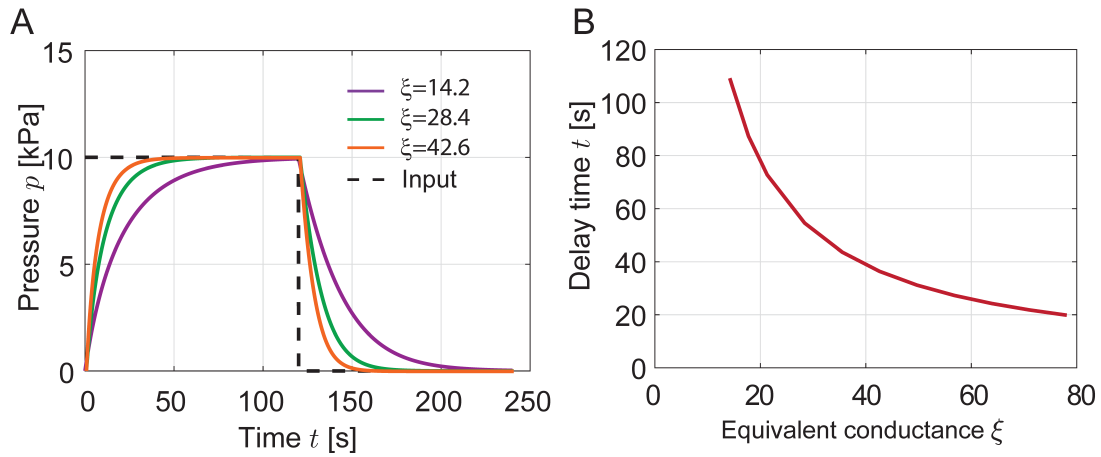


Fig. S15. Effect of the equivalent conductance ξ on the response of our viscous valves. (A) Numerically predicted pressure evolution at the inlet and outlet of a viscous valve characterized by $\xi = 14.2, 28.4$ and 42.6 when connected to the extension actuator considered in Fig. 1c. (B) Numerically predicted delay time between the input and output (i.e. the time that it takes p_{output} to reach p_{input}) as a function of ξ .

4. Additional Results

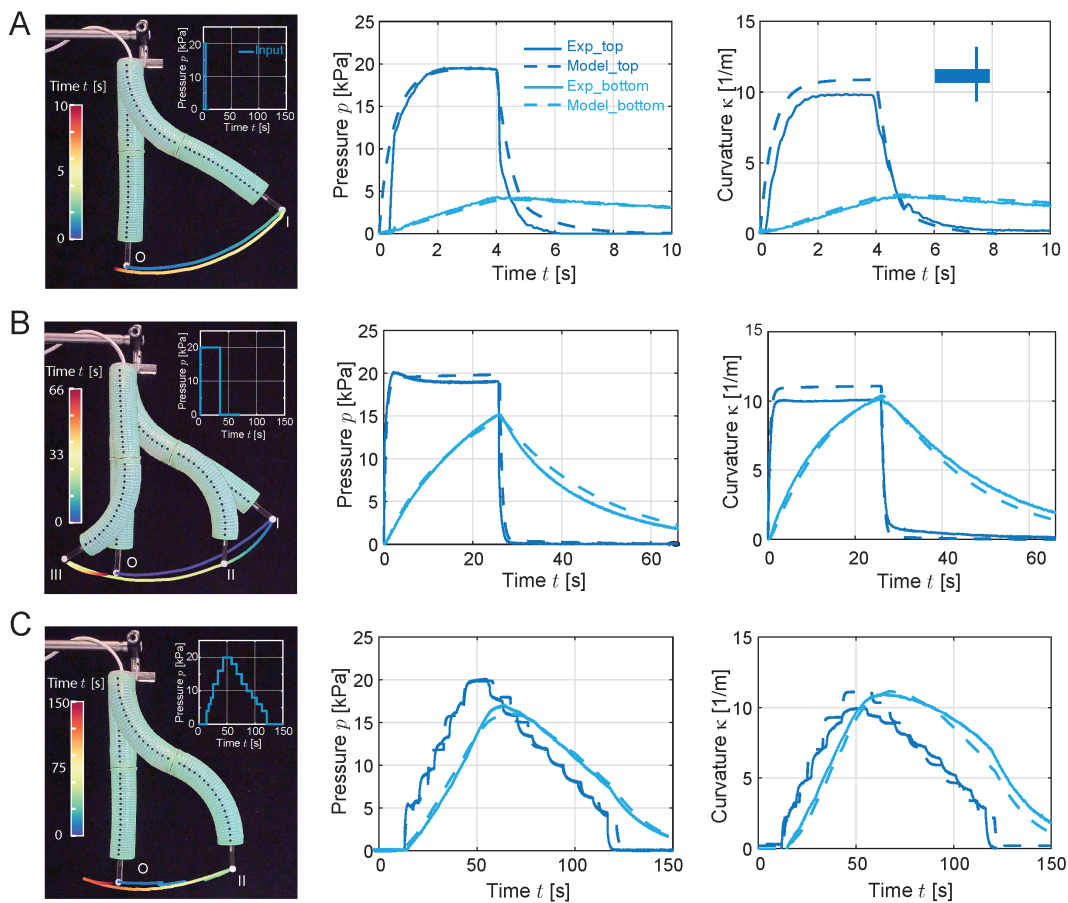


Fig. S16. Robotic arm comprising two bending actuators and a viscous valve. Multiple trajectories of the robotic arm are realized upon application of (A) a short rectangular pressure pulse ($p_{input} = 20$ kPa for $t_{input} = 4$ s), (B) a long rectangular pressure pulse ($p_{input} = 20$ kPa for $t_{input} = 26$ s) and (C) a gradually varied input pressure profile. Our model can accurately predict the pressure and curvature evolution of each actuator.

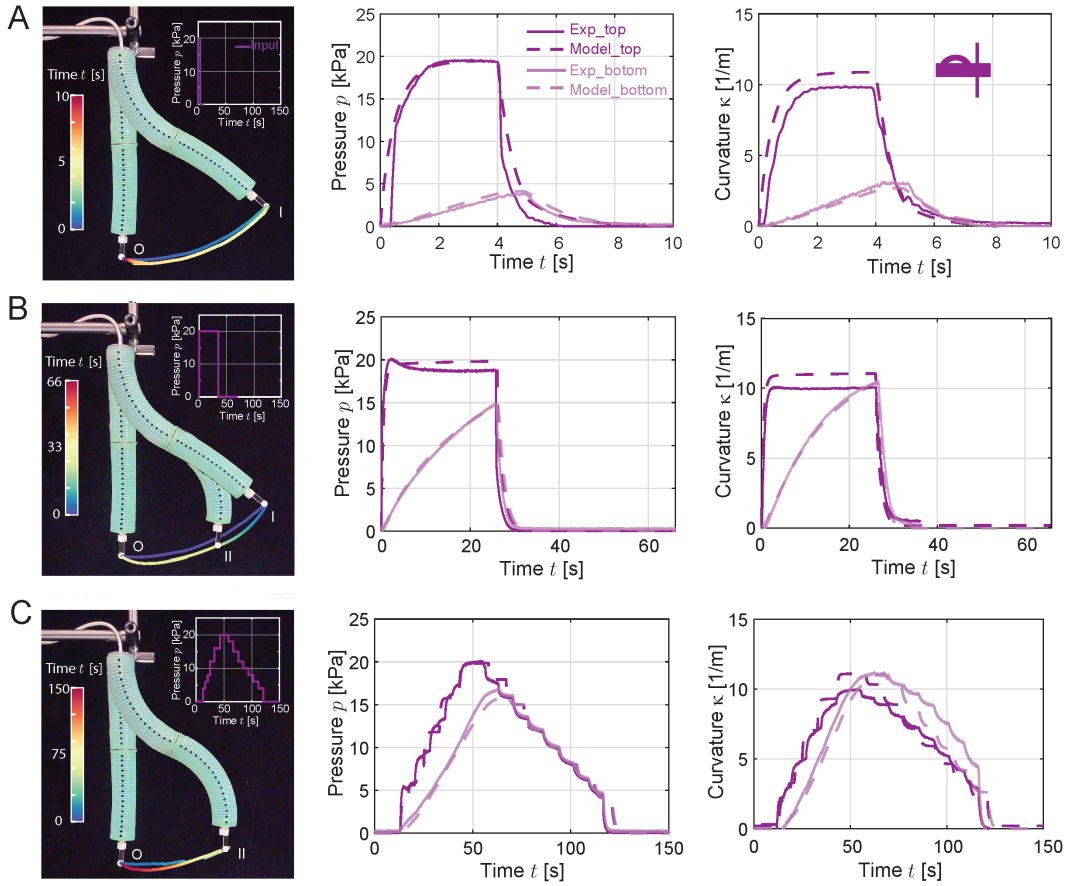


Fig. S17. Robotic arm comprising two bending actuators and a one-way viscous valve. Multiple trajectories of the robotic arm are realized upon application of (A) a short rectangular pressure pulse ($p_{input} = 20$ kPa for $t_{input} = 4$ s), (B) a long rectangular pressure pulse ($p_{input} = 20$ kPa for $t_{input} = 26$ s) and (C) a gradually varied input pressure profile. Our model can accurately predict the pressure and curvature evolution of each actuator.

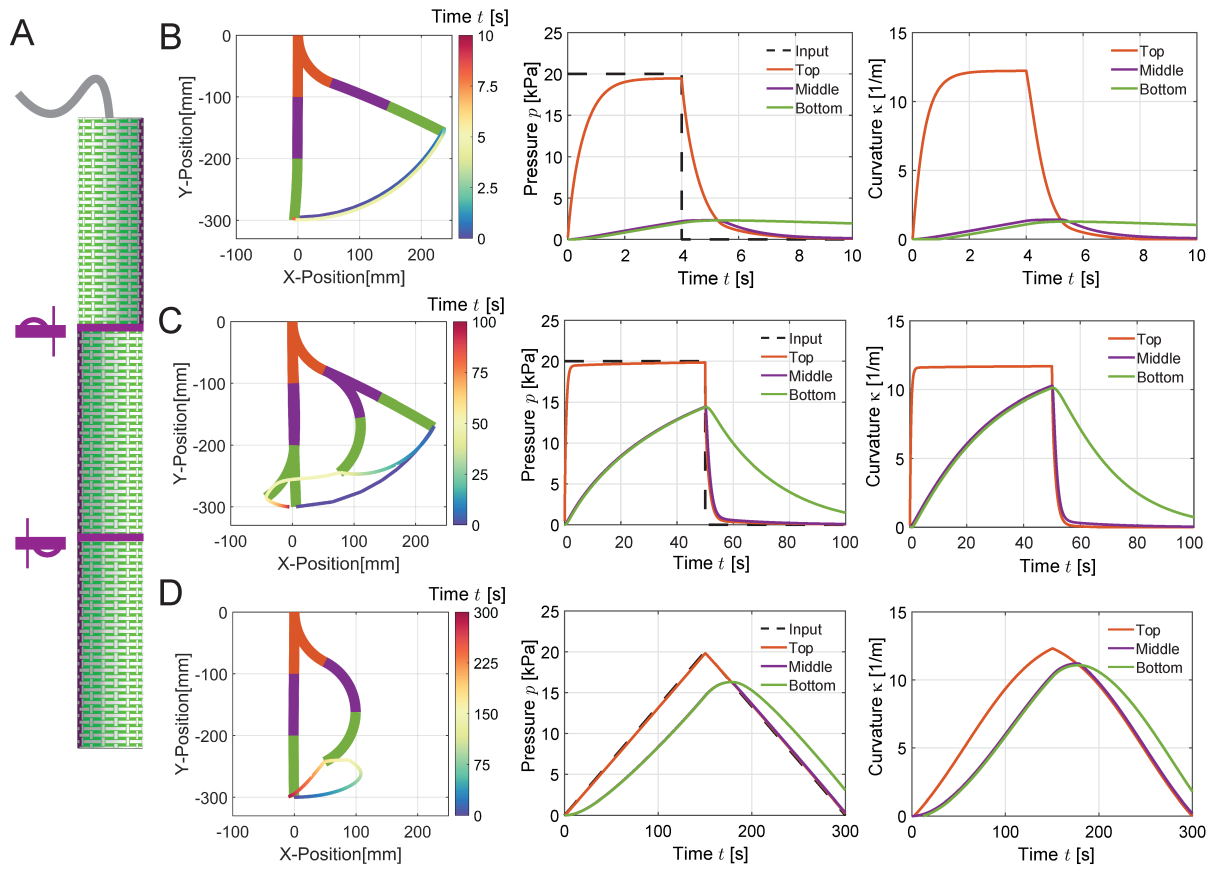


Fig. S18. Numerical results of a robotic arm comprising three bending actuators and two one-way viscous valves. (A) Schematic of the robotic arm. (B-D) Numerical results for the robotic arm upon application of (B) a short rectangular pressure pulse ($p_{input} = 20$ kPa for $t_{input} = 4$ s), (C) a long rectangular pressure pulse ($p_{input} = 20$ kPa for $t_{input} = 50$ s) and (D) a gradually varied input pressure profile.

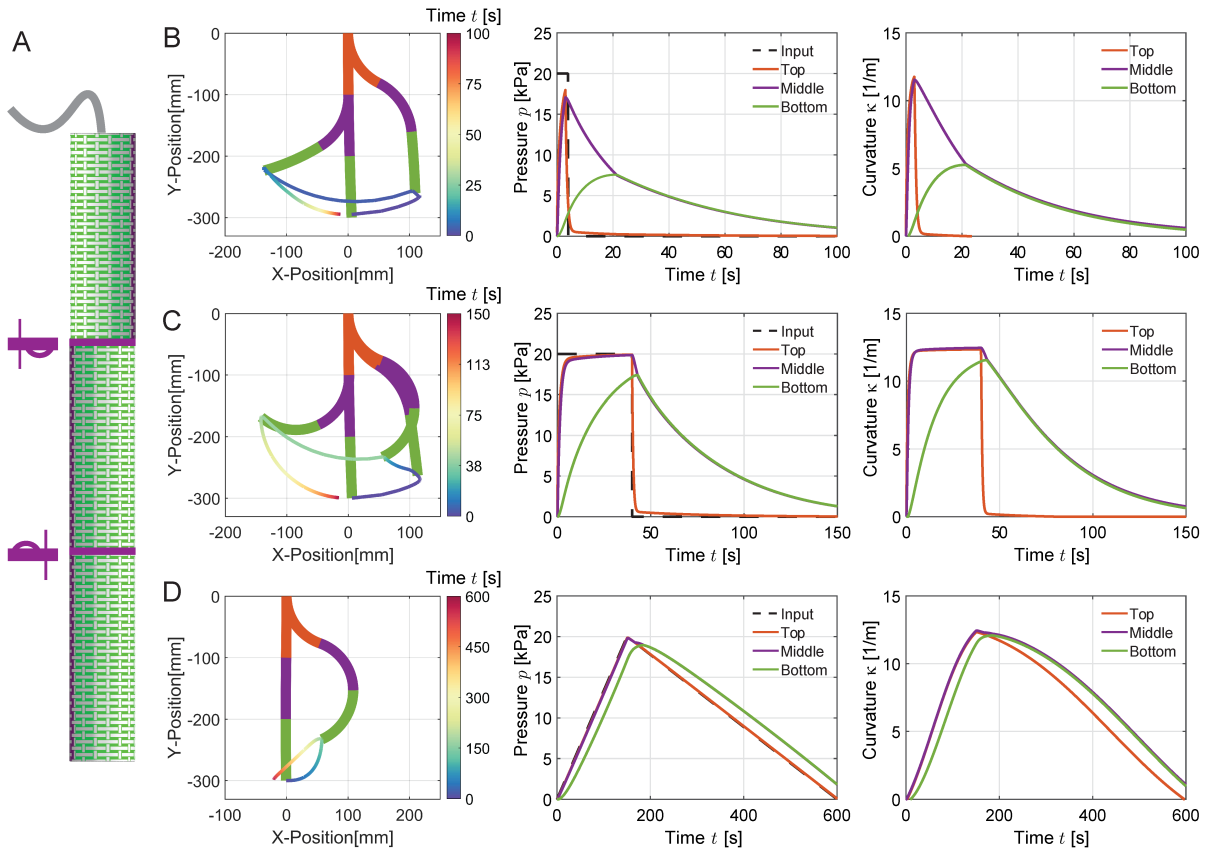


Fig. S19. Numerical results of a robotic arm comprising three bending actuators and two one-way viscous valves. (A) Schematic of the robotic arm. (B-D) Numerical results for the robotic arm upon application of (B) a short rectangular pressure pulse ($p_{input} = 20$ kPa for $t_{input} = 4$ s), (C) a long rectangular pressure pulse ($p_{input} = 20$ kPa for $t_{input} = 40$ s) and (D) a gradually varied input pressure profile. Note that this robotic arm is different from the one in Fig. S18 because of the flipped configurations of both viscous valves.

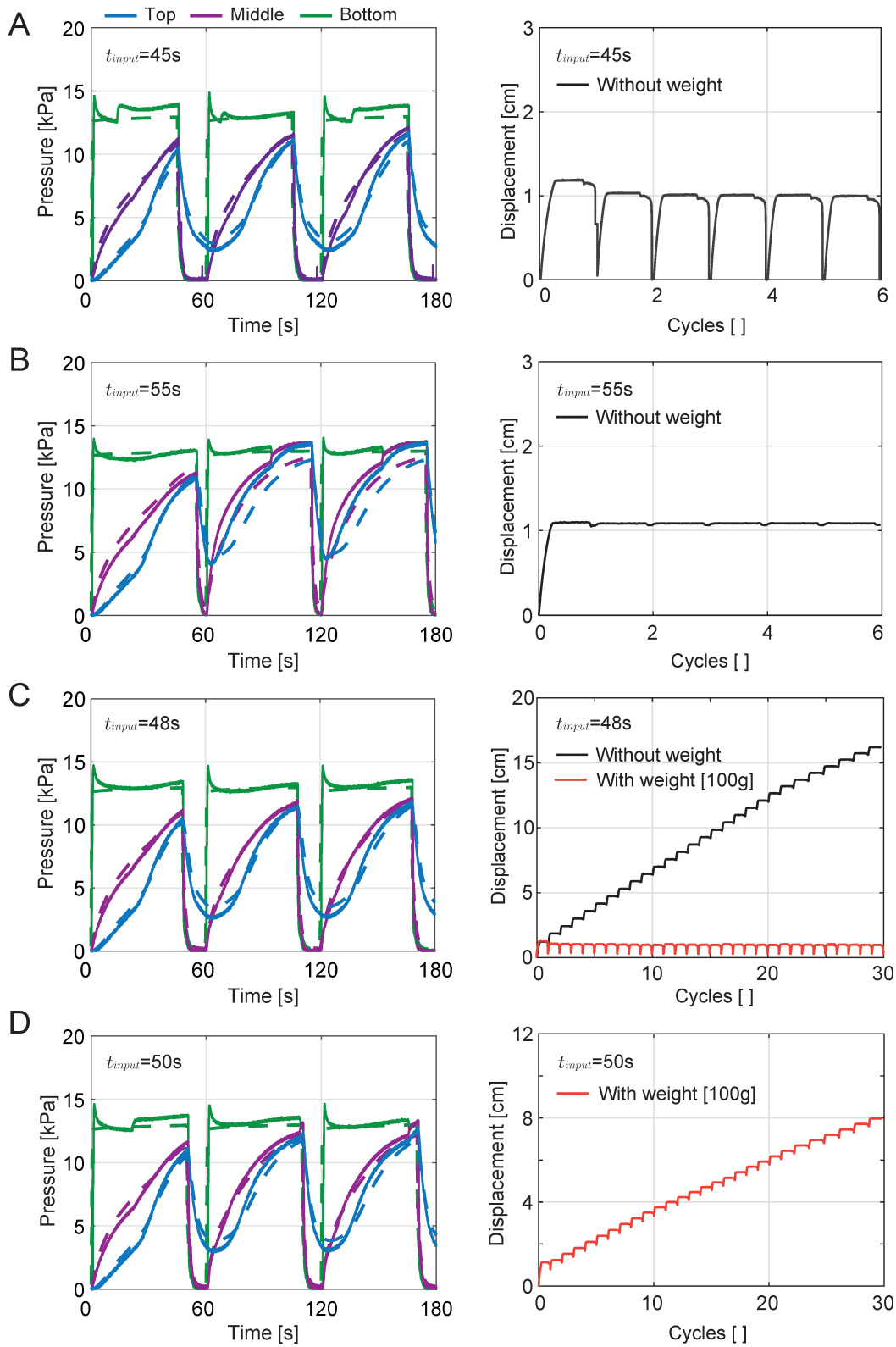


Fig. S20. Pressure evolution and displacements of the climbing robot upon application of a wide range of pressure inputs. (A) The robot falls down at the end of each cycle with $t_{input} = 45$ s. (B) The robot can not move upwards after the first cycle with $t_{input} = 55$ s. (C) The robot climbs up to 16 cm in 30 cycles but can not climb with additional weight (100 g) for $t_{input} = 48$ s. (D) The robot climbs up to 8 cm in 30 cycles with additional weight (100 g) with $t_{input} = 50$ s.

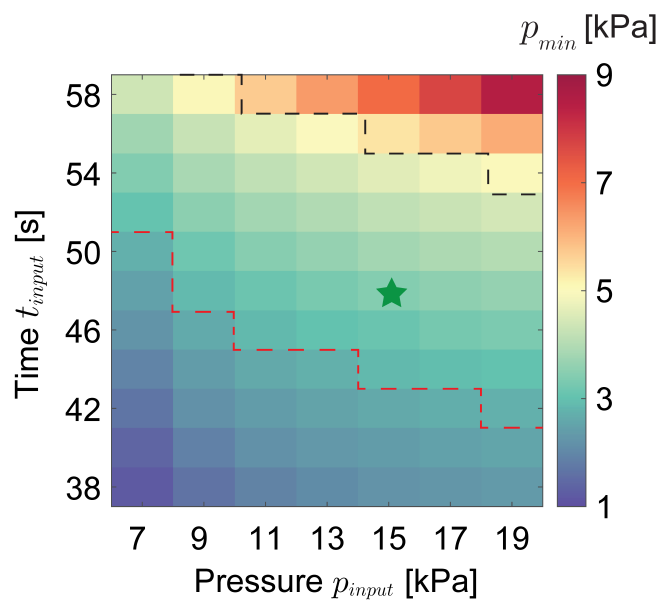


Fig. S21. Phase diagram of the minimum pressure inside the climbing robot's top actuator when a hysteretic valve is embedded into it. The embedded hysteretic valve affects the cavity of the top actuator and, in turn, the pressure-volume evolution. The area of the diagram that is bounded by the two dashed lines identifies the input parameters for which the robot will achieve climbing. Guided by our model, we choose $p_{input} = 48$ s and $p_{input} = 15$ kPa as the input for the grasping tests.

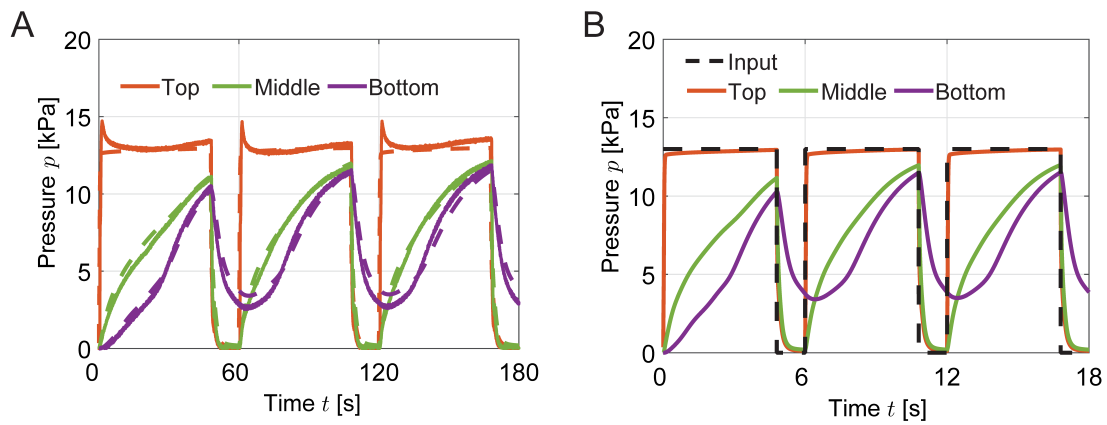


Fig. S22. Effect of the equivalent conductance of both the pump and the valves on actuation speed. (A) Pressure evolution inside the three actuators for the climbing robot considered in Fig. 3 of the main text. (B) Numerically predicted pressure evolution inside the three actuators for a climbing robot for which the equivalent conductance ξ of both the pump and the valves is increased by 10 times.

422 **Movie S1. Characterization of the mechanical valves.**

423 To demonstrate the capabilities of our mechanical valves, we connect each valve to an extending
424 actuator and compare the pressure evolution at the inlet and outlet of the valve.

425

426 **Movie S2. Robotic arm with different trajectories.**

427 The robotic arm consists of two bending actuators and a viscous valve (or one-way viscous valve).
428 It is capable of achieving multiple trajectories with a single pressure input.

429

430 **Movie S3. Tube climbing robot.**

431 The climbing robot consists of two expanding actuators, an extending actuator, a viscous valve
432 and a one-way viscous valve. It can climb inside a pipe carrying two times its own weight. When a
433 threshold valve and a gripper are integrated in the robot, the robot can also grasp an object and
434 pull it down. All the movements are achievable with a single pressure input.

435

436 **Movie S4. Rolling robot.**

437 The hexagonal rolling robot comprises 12 inflatable chambers and six viscous valves arranged
438 into two circuits. A bistable valve activates one circuit at a time, enabling the robot to successfully
439 navigate in both directions with a single input.

440

441 **References**

442 1. Jin L, Forte AE, Deng B, Rafsanjani A, Bertoldi K (2020) Kirigami-inspired inflatables with
443 programmable shapes. *Advanced Materials* 32(33):2001863.

444 2. Ilievski F, Mazzeo AD, Shepherd RF, Chen X, Whitesides GM (2011) Soft robotics for chemists.
445 *Angewandte Chemie* 123(8):1930–1935.

446 3. Senn M (2021) Digital image correlation and tracking: Calculate displacement, strain and
447 stress from image sequences. *MATLAB Central File Exchange*. [https://www.mathworks.com/
448 matlabcentral/fileexchange/50994-digital-image-correlation-and-tracking](https://www.mathworks.com/matlabcentral/fileexchange/50994-digital-image-correlation-and-tracking).

449 4. Pratt V (1987) Direct least-squares fitting of algebraic surfaces. *ACM SIGGRAPH computer
450 graphics* 21(4):145–152.

451 5. Chernov N (2021) Circle fit (pratt method). *MATLAB Central File Exchange*. [https://www.
452 mathworks.com/matlabcentral/fileexchange/22643-circle-fit-pratt-method](https://www.mathworks.com/matlabcentral/fileexchange/22643-circle-fit-pratt-method).

453 6. Vasios N, Gross AJ, Soifer S, Overvelde JT, Bertoldi K (2020) Harnessing viscous flow to simplify
454 the actuation of fluidic soft robots. *Soft Robotics* 7(1):1–9.